High pressure trace element partitioning between clinopyroxene and alkali basaltic melts

Barbara Bonechi [a], Cristina Perinelli [a], Mario Gaeta [a], Alessandro Fabbrizio [b], Maurizio Petrelli [c], Ladislav Strnad [d]

a: Dipartimento di Scienze della Terra, Sapienza Università di Roma, P. le Aldo Moro 5, 00185, Rome, Italy

b: Institute of Petrology and Structural Geology, Faculty of Science, Charles University, Albertov 6, 12843 Prague, Czech Republic

c: Department of Physics and Geology, University of Perugia, Piazza Università, Perugia 06100, Italy

d: Laboratories of the Geological Institutes, Charles University, Albertov 6, Prague 2, CZ-12843, Czech Republic

Corresponding author:

Barbara Bonechi

Dipartimento di Scienze della Terra, Sapienza Università di Roma,

P. le Aldo Moro, 5 00185 Rome, Italy

E-mail: barbara.bonechi@uniroma1.it

ORCID: 0000-0002-0242-4320

Abstract

We present new experimental data on major and trace element partition coefficients (*D*) between clinopyroxene and a K-basaltic melt from Procida Island (Campi Flegrei Volcanic District, south Italy). Time-series experiments were conducted at 0.8 GPa and 1080-1250 °C aiming to investigate the role of the crystallization kinetics on trace elements partitioning behaviour at a pressure relevant for deep magmatic reservoirs. Results indicate that large ion lithophile elements (LILE) are incompatible (e.g., $D_{Sr} \leq 0.15$), light rare elements (LREE; e.g., $D_{La} \leq 0.20$) are always more incompatible than heavy rare elements (HREE), which in some cases result to be compatible with clinopyroxene (e.g., $D_{Dy} = 1.40$); high field strength elements (HFSE) are generally incompatible ($D_{HFSE} \leq 0.8$), while transition elements (TE) range from slightly incompatible (e.g., $D_{V} = 0.6$) to highly compatible (e.g., $D_{Cr} = 63$). The calculated *D* values for LILEs, REEs, HFSEs, and TEs tend to decrease with the increase of temperature and to increase with increasing tetrahedrally-coordinated aluminium content, in agreement with the previous studies. Moreover, we observed the influence of the growth rate on the partition coefficients, with the highest D_{REE} values calculated in the runs with the highest growth rate (~10^{-7} cm s^{-1}), due to the less efficient rejection of incompatible elements during rapid crystal growth, that in this study is not linked to disequilibrium conditions, but to the presence of pre-existing nuclei. Additionally, the apparent increase in D_{REE} values with time observed in some runs is not referable to a change in time but rather to the different degrees of polymerization, expressed as the ratios NBO/T of these melts, strictly related to a loss of Fe occurred during the experiments, and thus to a different melt viscosity. Finally, the application of the experimental clinopyroxene/melt partition coefficients highlights that the deepest step of the magmatic differentiation in the Campi Flegrei Volcanic District is represented by the fractionation of about 20-30% of a clinopyroxenitic mineral assemblage from a basaltic parental magma.

Keywords: clinopyroxene; trace element partition coefficient; lattice strain model; order-disorder crystal growth; fractional crystallization

1. Introduction

A central factor in the evolution of an igneous body is the partitioning of elements between the melt and the crystallizing minerals. The partition coefficient of an element *i* (D_i) has been defined as its concentration in a mineral divided by the concentration of that element in the coexisting melt (Beattie et al., 1993) and describes the chemical distribution between coexisting phases under equilibrium conditions. Most partition coefficients, indeed, are usually investigated presupposing equilibrium conditions, assuming thus that natural systems are characterized by chemical homogeneity of melt and crystals and that these systems evolve slowly enough to allow for continuous re-equilibration between melt and growing crystals (e.g., Onuma et al., 1968; Higuchi and Nagasawa, 1969; Philpotts and Schnetzler, 1970; Schnetzler and Philpotts, 1970). However, disequilibrium conditions are not unusual in natural systems, potentially affecting both absolute and relative partition coefficients, as observed by Albarede and Bottinga (1972). The resulting disequilibrium partition coefficients can be used as sensitive monitors of magmatic processes such as fractional crystallization, assimilation, mixing and partial melting of crustal or mantle rocks (e.g., Leeman and Phelps, 1981; Mahood and Hildreth, 1983; Drexler et al., 1983; White, 2003; Henderson and Pierozynski, 2012; Arzilli et al., 2018). Indeed, as shown in several studies, in some natural igneous systems, events of rapid crystal growth (driven by the undercooling degree) can produce an excessive accumulation or depletion of trace elements, depending on their degree of compatibility or incompatibility, at the crystal-melt interface with a consequent disequilibrium element uptake during crystal growth (e.g., Albarede and Bottinga, 1972; Watson, 1996; Morgan and London, 2003; Watson and Müller, 2009; Mollo et al., 2011, 2013; Arzilli et al., 2018) with respect to equilibrium conditions (e.g., Morgan and London, 1996; Lofgren et al., 2006; Mollo et al., 2011, 2013). Therefore, trace elements partitioning can be controlled by kinetic effects such as diffusive re-equilibration and undercooling degree (Arzilli et al.,

2018; Shea et al., 2019) as well as by temperature and pressure (Shimizu, 1974; Green and Pearson, 1983; Ray et al., 1983; Green and Pearson, 1985; Gallahan and Nielsen, 1992; Jones, 1995; Blundy and Wood, 2003; McDade et al., 2003; Sun and Liang, 2012; Yao et al., 2012; Bédard, 2014; Mollo et al., 2018), mineral composition (Yagi and Onuma, 1967; Onuma et al., 1968; Colson et al., 1988; Blundy and Wood, 1991, 1994; Skulski et al., 1994; Lundstrom et al., 1998; Hill et al., 2000; Bédard, 2010; Mollo et al., 2016), melt composition (Mysen and Virgo, 1980; Ray et al., 1983; Nielsen, 1985; Gallahan and Nielsen, 1992; Bennett et al., 2004; Gaetani, 2004), and redox conditions (Aigner-Torres et al., 2007; Cartier et al., 2014; Dygert et al., 2020). Among the works focused on the influence of the crystallization kinetics on partition coefficients (Albarede and Bottinga, 1972; Morgan and London, 2003; Lofgren et al., 2006; Milman-Barris et al., 2008; Mollo et al., 2011, 2013; Arzilli et al., 2018; Shea et al., 2019), only a few have focused on clinopyroxene (Shimizu, 1981; Lofgren et al., 2006; Mollo et al., 2013). The work of Shimizu (1981) investigates kinetic effects on sector-zoned augite phenocrysts showing a clear case of disequilibrium crystallization. Lofgren et al. (2006) performed equilibrium and dynamic crystallization experiments at cooling rates in the range 5-1000 °C/h to explore the effects of kinetics on *D*-values. Mollo et al. (2013) determined trace element partition coefficients at the interface between clinopyroxene rims and co-existing glasses resulting from isothermal and cooling rate experiments. The study of the factors influencing trace element partitioning is of paramount importance since the latter are frequently used in petrological and geochemical studies to better understand magmatic processes, like fractional or equilibrium crystallization, assimilation, and partial melting (e.g., Mollo et al., 2016). This is because clinopyroxene has crystal-melt REE partition coefficients approximately up to 4 orders of magnitude higher than other mafic rock-forming minerals (e.g., olivine and orthopyroxene; Chen and Zhang, 2009; Sun, 2018). Clinopyroxene therefore, exerts a strong control on the overall partitioning of the crystallising assemblage. In this study, we present a new set of partition coefficient data derived from synthetic clinopyroxenes in equilibrium and in disequilibrium with a K-basaltic composition from the Campi Flegrei Volcanic District (CFVD) as a function of temperature and time. The investigated

pressure of 0.8 GPa represents the depth of the crustal-mantle boundary in the CFVD area (~25 km of depth; Fedi et al., 2018). Complementing our experimental data, we also measured the trace element concentrations in some natural clinopyroxene phenocrysts belonging to scoria clasts from Procida island in the CFVD. The main aim of this work, indeed, is to address: *i*) the scarcity of quantitative experimental data on the role of the crystallization kinetics on clinopyroxene-melt trace elements partitioning behaviour at high-pressure conditions relevant for deep magmatic reservoirs; *ii*) the absence of clinopyroxene-melt partition coefficient experimental data for primitive compositions in the CFVD area. Based on the evidence relating to the stages of deep crystallization of the Campi Flegrei Volcanic District parental magmas (Di Stefano et al., 1999; Piochi et al., 2005; Chiarabba et al., 2008; Mormone et al., 2011; Moretti et al., 2013; Fedi et al., 2018), we explored the mineral assemblage involved in the magmatic differentiation at the deepest ponding level, applying the experimental results of this study.

2. Methods

2.1. Samples description

Synthetic samples were obtained through crystallization experiments performed by using the ½ inch end loaded piston cylinder apparatus at the HP-HT Laboratory of the Earth Sciences Department (Sapienza University, Rome, Italy) at 0.8 GPa, 1080-1250 °C, $1 \leq H_2O \leq 4$ wt.%, with durations of 0.25, 3, 6 and 9 hours. For these experiments we used two different starting materials: the APR16 powder and the APR16GL glass (Table 1), both obtained from a natural primitive K-basalt (APR16 sample) found as scoria clast in the deposits of the Solchiaro hydromagmatic eruption (~22 ka ago; (Morabito et al., 2014) located in Procida Island (Campi Flegrei, Italy). This K-basalt is characterized by 12 vol.% of forsteritic olivine and diopsidic clinopyroxene phenocrysts dispersed in a groundmass made of olivine, clinopyroxene, plagioclase, Ti-magnetite, alkali feldspar and glass (D'Antonio et al., 1999; De Astis et al., 2004). The APR16 powder, previously used as starting material in the experimental runs of Bonechi (2020) (Table 2), was obtained by grinding the natural APR16 rocky

sample in an agate mortar under acetone. The APR16GL, instead, used as starting material in the runs of Bonechi et al. (2020b) (Table 2), was prepared by melting for 15 min the APR16 natural powder in a 1 atm gas-mixing (CO-CO_2) furnace installed at the Bayerisches Geoinstitut (Bayreuth, Germany) at 1400 °C and oxygen fugacity corresponding to the NNO (nickel-nickel oxide) buffer. Then, the obtained glassy starting material was grinded in an agate mortar under acetone. Compositions of synthetic clinopyroxenes were compared with natural clinopyroxene phenocrysts occurring in the SCE and SOG scoria clasts, belonging to the Solchiaro eruption. The SCE and SOG samples (Table 1 and Supplementary Material 1) are porphyritic, scarcely vesiculated rocks containing ~10-20 vol.% of medium-grained olivine and clinopyroxene phenocrysts (olivine/clinopyroxene ratio ~1). A detailed description of these samples is reported in Bonechi et al. (2020b).

2.2. Experimental techniques

The detailed experimental procedure is described by Perinelli et al. (2019) and by Bonechi et al. (2020a, 2020b). Here we report the main aspects. Assemblies made of CaF_2 outer sleeve, graphite furnace and crushable magnesia spacers were used. The friction correction factor associated with our assembly was determined to be ~6% through the calibration based on the reaction fayalite + quartz = ferrosilite at the fixed temperature of 1000 °C; at this temperature, the reaction takes place at approximately 1.4 GPa (Bohlen et al., 1980).

The experimental charges were prepared loading $Au_{75}Pd_{25}$ capsules with ~40 mg of sample powder. For hydrous experiments we added water in known amounts by using a 1.0 μL microsyringe (Table 2). Loss of H_2O by vaporization during welding was prevented by freezing the crucible with nitrogen. The welded capsule was weighed, stored in a furnace at 110 °C, and then weighed again to confirm the absence of water leaks. Moreover, to minimise possible loss of H_2 during the experiments the charges were surrounded by pyrophyllite powder (Freda et al., 2001). Temperature was controlled by a factory calibrated W_3Re_{97}-$W_{25}Re_{75}$ (type D) thermocouple and maintained with an uncertainty of ±

5 °C. For the experimental run-up we used the "hot piston-out" procedure (Johannes et al., 1971; Presnall et al., 1978) modified consisting in the first cold pressurization of the assembly to a value ~ 10% over the target pressure and then the sample was heated to the final run temperature. This technique allows to closely approach the run pressure through the stress relaxation within the assembly upon heating, requiring only minor upward pressure adjustments during the experiment in most cases (Watson et al., 2002). The heating rate was imposed at 150 °C/min. The sample was maintained at the pressure and temperature for a given duration (nominal duration), and then quenched by turning off the power. The temperature drop below 500 °C was of <5 s (average cooling rate of 150 °C/s). All the runs were self-buffered; an estimation of experimental oxygen fugacity (fO_2) was made through the equation of Kress and Carmichael (1991). To use this equation, where possible, we first assessed the FeO content of experimental residual glass, and then its Fe^{2+}/Fe_{tot} mole ratio; to do this we used the value of iron and magnesium partitioning between olivine and liquid (K_D Fe-Mg ol/liq) calculated according to the procedure proposed by Toplis (2005). Therefore, the application of Kress and Carmichael (1991) equation residual glass of each experiment, yielded fO_2 values between of -1.9 and +0.9 log-bar units with respect the nickel-nickel oxide buffer. As a whole the estimated range of fO_2 value is in agreement with those estimated for similar furnace assemblages (Conte et al., 2009; Weaver et al., 2013; Perinelli et al., 2019; Bonechi et al., 2020a). Finally, we determined the effective undercooling (ΔT_{eff}) that is the difference between the equilibrium clinopyroxene liquidus temperature (TCpx$_L$) and the experimental temperature (Bonechi et al., 2020b, 2020a; Bonechi, 2020). For calculations, TCpx$_L$ value of APR16-NWA experiments was taken from Procida K-basalt experimental data (i.e., 1270 °C; see Table 2 in Perinelli et al., 2019) whereas TCpx$_L$ values of APR16GL experiments were calculated by the MELTS software (Ghiorso and Sack, 1995; Asimow and Ghiorso, 1998) using 0, 2 and 4 wt% as initial water contents (i.e., H_2O_i in Table 2).

2.3. Analytical techniques

2.3.1. Textural investigations and major element determinations

Back-scattered electron (BSE) images used to investigate textural aspects of both natural and experimental samples were collected by Scanning Electron Microscopy (SEM) using a FEI-quanta 400 equipped for microanalysis with an EDAX Genesis system at the Earth Sciences Department, Sapienza University of Rome. Major elements were analysed at the CNR-Istituto di Geologia Ambientale e Geoingegneria di Roma, with a Cameca SX50 electron microprobe equipped with five wavelength dispersive spectrometers (WDS). Quantitative analyses were performed using 15 kV accelerating voltage and 15 nA beam current. As standards we employed metals for Mn and Cr, Jadeite for Na, Wollastonite for Si and Ca, Orthoclase for K, Corundum for Al, Magnetite for Fe, Rutile for Ti, Periclase for Mg, Apatite for P. Counting times for all elements were 20 s on peak and 10 s on both backgrounds. Light elements (Na, K) were counted first to prevent loss by volatilization. The PAP correction method was used. Minerals were analysed using a beam diameter of 1 μm whereas to minimize alkali loss during glass analysis, the beam was defocused to 15 μm. In order to evaluate the accuracy of the analyses, repeated analyses of three international secondary standards (Kakanui augite, Iceladic Bir-1 and rhyolite RLS132 glasses from USGS) were made prior to any series of measurements. The mean precision from the standard value was about 1% for SiO_2, 2% for Al_2O_3, 5% for K_2O, CaO and FeO, and 8-10% for other elements. The analytical precision (2 sigma error) is ≤ 1% for elements in the concentration range >10 wt% oxide, 5% for elements in the range 2–10 wt% oxide and better than 10% for elements in the range 0.5–2 wt% oxide. The water contents of experimental glasses were estimated according to the by-difference method (Devine et al., 1995; Humphreys et al., 2006). We are aware that this method is not fully reliable given the estimation is affected by i) element concentrations not measured by EMPA and ii) surface charge effects (Hughes et al., 2019) leading to an overestimation of H_2O concentration. However, the obtained H_2O values show a good linear correlation (correlation coefficient $R^2 = 0.97$) with are close to those determined by micro-Raman spectroscopy measurements on residual melts of equilibrium experiments performed on the same composition, at the same *P*, *T* and initial hydrous conditions (see Perinelli et al., 2019, for details).

208

209 *2.3.2. Laser ablation-inductively coupled plasma mass spectrometry (LA-ICP-MS)*

210 LA-ICP-MS analyses were performed on both natural (SCE and SOG samples) and experimental
211 samples. LA-ICP-MS analyses of SCE and SOG natural samples were performed on a quadrupole–
212 based ICP-MS iCAP-Q instrument (Thermo Fisher Scientific, Bremen) coupled to a modified
213 NewWave UP 213 laser microprobe (NewWave, USA) installed at Charles University, Prague.
214 Analyses of natural clinopyroxene crystals were performed using a circular laser beam of 100 μm
215 diameter, a frequency of 10 Hz and a laser density on the sample surface of 3.5 J/cm^2. External
216 calibration of the laser ablation analyses was done using Standard Reference Materials NIST
217 (National Institute of Standards and Technology, USA) 612 with internal standardisation using Si,
218 based on electron microprobe measurements. The concentration values for NIST of all measured
219 elements were taken from (Pearce et al., 1997). The external reproducibility of this method was
220 checked on repeated analyses of USGS BCR-2G glass as reference material (e.g., Strnad et al., 2005
221 and reference therein; Table S1 in Supplementary Material 2). The isotopes used were selected with
222 respect to their most abundant species, free from isobaric overlap and minimum interferences.
223 Formation of oxides (MO^+/M^+) was monitored using U in NIST 612 directly from ablation and the
224 measured ratios ($^{254}UO^+/^{238}U^+$) was below 10^{-2}. Further details about the analytical protocol and
225 correction strategy have been described by Strnad et al. (2005) and Skála et al. (2009). Detection
226 limits for all elements were calculated as 3σ level of the gas blank (Table S1 in Supplementary
227 Material 2). LA-ICP-MS analyses of the experimental samples were performed at the Department of
228 Physics and Geology, University of Perugia (Italy). The instrumentation consisted of a
229 Teledyne/Photon Machine G2 LA device equipped with a Two-Volume ANU HelEx 2 cell coupled
230 with a Thermo Fisher Scientific quadrupole-based iCAP-Q ICP-MS. Analyses of clinopyroxene
231 crystals and glasses were performed using a circular laser beam of 8-20 μm diameter, a frequency of
232 10-15 Hz and a laser density on the sample surface of 3.5 J/cm^2. Oxide formations was measured on
233 the NIST SRM 612 monitoring and maintaining the ratio ThO/Th below 0.005. The NIST SRM-610

234 standard reference material was used as calibrant and Ca, previously analysed by EPMA, as internal
235 standard. Under these operating conditions precision and accuracy are better than 10% for most of
236 the elements (Petrelli et al., 2007, 2008, 2016). In detail, at beam sizes equal or larger than 15 μm,
237 precision (measured as one sigma) and accuracy (expressed as relative deviation from the reference
238 value) are of the order of 10% (Petrelli et al., 2016). At a smaller beam size of 8 μm, precision
239 decreases to 15% for concentration above 1.7 μg g^{-1} (Petrelli et al., 2016). Accuracy is better or equal
240 to 10% and 13% at beam sizes of 15 and 10 μm, respectively (Petrelli et al., 2016). When the spatial
241 resolution is increased to 8 μm, accuracy remains better than 15% (Petrelli et al., 2016).
242
243 **3. Results**
244 ***3.1 Phase relations***
245 Experimental samples investigated in this study are described in detail in previous works dealing with
246 phase equilibria and crystallization kinetics in the APR16 K-basalt (Perinelli et al., 2019; Bonechi et
247 al., 2020b, 2020a; Bonechi, 2020). Here we briefly report a description of the paragenesis of these
248 samples given the importance of the coexistence of several phases for the fractionation of some trace
249 elements, like the presence of plagioclase for the fractionation of Eu. Overall, the experimental
250 products consist of glass and microlites of clinopyroxene (Cpx) ± olivine (Ol) ± plagioclase (Plg) ±
251 oxide (Ox). In particular, the APR16-1C and APR16-35 runs (1225 °C), performed using the natural
252 starting material APR16, are characterized by the presence of glass (Gl) and Cpx plus restitic Ol and
253 Ox. In the runs performed at 1250 °C (APR16-C1Ac and APR16-C1Ad), the dominant phase is Cpx
254 while olivine (Ol) crystallizes only in the APR16-C1Ac run. The mineral phases crystallized in the
255 runs at 1220 °C (APR16-C2Aa, APR16-C2Ab, APR16-C2Ac, APR16-C2Ad) are Cpx + Ol + Plg +
256 Ox. Clinopyroxene and Ol are ubiquitous in these runs, whereas Plg is present only in the runs at 3
257 and 6 hours (i.e., APR16-C2Ab, APR16-C2Ac) and Ox is absent in the run APR16-C2Ac. The runs
258 at 1170 °C (APR16-C2Bc and APR16-C2Bd) show a higher degree of crystallization and the mineral
259 assemblage is Cpx + Ol + Plg ± Ox. Finally, the hydrous run at 1080 °C (APR16-C3Ac; 6.5 wt.%

H_2O) shows a degree of crystallization similar to that of the runs at 1170 °C and the phases crystallized are Cpx and Ol.

3.2. Texture and chemical composition of experimental samples

Clinopyroxene. Chemical compositions of Cpx are given in Table S2 in Supplementary Material 2. Overall synthetic Cpx crystals are characterized by homogeneous composition and euhedral habits (Fig. 1a-c). In particular, in the runs performed using the glassy starting material (i.e., APR16GL) habit and sizes vary with time: subhedral with sizes of ~5-10 μm in the shortest run (e.g., APR16-C2Aa; 0.25 h; Fig.1a) and euhedral with sizes up to ~20 μm in the longest run (≥ 3 h; Fig. 1b). The runs APR16-1C and APR16-35, performed using the natural starting material (i.e., APR16 natural powder), instead, are characterized by euhedral habit and sizes up to ~50 μm (Fig. 1c) (Bonechi, 2020). These Cpx crystals are augitic ($Wo_{42}En_{41}Fs_{18}$) and diopsidic ($Wo_{47}En_{43}Fs_{10}$) in composition according to the classification scheme of Morimoto et al. (1998) (Fig. 2a). Overall, the Mg# of Cpx (calculated as the molar $MgO/(MgO+FeO_{tot})$ ratio) varies between 0.81 and 0.92, the TiO_2 contents are between 0.58 and 1.18 wt.% while those of Al_2O_3 are between 5.00 and 9.49 wt.%. The Fe–Mg distribution coefficients between clinopyroxene and melt ($K_D(Fe\text{-}Mg)^{Cpx\text{-}liq} = Fe_{Cpx}\times Mg_{liq}/Mg_{Cpx}\times Fe_{liq}$, calculated assuming all Fe as Fe^{2+} in both phases), for the longest runs ≥ 3 hours lie in the equilibrium range of 0.28±0.08 (Putirka, 2008) whereas the shortest experiment (APR16-C2Aa) shows significant deviation from the equilibrium (Table S2 in Supplementary Material 2).

Glass. Chemical compositions of experimental glasses are given in Table S3 in Supplementary Material 2. Glass composition of anhydrous and hydrous experiments varies from K-basalt to K-trachybasalt up to shoshonite compositions with decreasing temperature (Fig. 2b). In particular, in the anhydrous runs, before reaching the temperature at which plagioclase significantly crystallizes, the glass composition is controlled by clinopyroxene crystallization thus leading to a very limited SiO_2 increase in the residual glasses (Perinelli et al., 2019). In the hydrous experiments, the earlier

crystallization of olivine ± spinel causes a slightly more marked increase of SiO_2 abundance in the residual glasses (from ~52 to ~53 wt.%; Table S3 in Supplementary Material 2).

3.3. Trace and REE content

Average compositions of trace elements concentrations analysed by LA-ICP-MS technique in synthetic clinopyroxene and coexisting glass are reported in Table 3.

3.3.1. Clinopyroxene

Figure 3 shows the trace elements concentrations in synthetic and natural clinopyroxene normalized to chondrite C1 after Anders and Grevesse (1989) for LILEs (Large-Ion Lithophile Elements), REEs + Y (Rare Earth Elements plus Yttrium), HFSEs (High Field Strength Elements) and TEs (Transition Elements). In this diagram some LIL elements (e.g., Rb and Ba) of synthetic Cpx crystals display different relative abundances depending on experimental conditions unlike the REEs that instead, show quite uniform high contents. In particular, the chondrite-normalised REE patterns have a general L/HREE (Light/Heavy rare earth element) enrichment (i.e., La_N/Yb_N = 0.85-1.20, where the subscript *N* denotes chondrite-normalized values) with a maximum at Sm_N (~20-37). The REE profiles from the crystallized cpx are comparable to each other with the exception of the clinopyroxene in the APR16-C2Bd charge that shows an evident Eu negative anomaly (Eu/Eu* = 0.58; Eu/Eu* = $Eu_N/(Sm_N \times Gd_N)^{1/2}$), likely due to the crystallization of plagioclase in this run. Indeed, the lack of plagioclase in the hydrous experiment APR16-C3Ac, justifies the absence of troughs at Eu (Eu/Eu* = 0.95), despite both crystallization degree and amount of Cpx crystallized in this experiment are similar to that of APR16-C2Bd run (40 wt.% and 43 wt.%, and 33 wt.% and 34 wt.%, respectively; Table 2). Finally, tetravalent HFSEs (i.e., Zr and Hf) have a higher concentration than pentavalent cations (i.e., Ta and Nb), while as regards TEs, it is possible to see evident troughs at Co and Ni.

3.3.2 Glass

Figure 4 shows the trace elements concentration in the experimental glasses normalized to chondrite C1 after Anders and Grevesse (1989) for LILEs, REEs + Y, HFSEs and TEs. Generally, all the experimental glasses match the trend of the APR16 sample (Mazzeo et al., 2014), with evident troughs at Pb, Co and Ni. C1-normalized trace element diagrams are L-MREE (Light/Middle rare earth element) enriched (La_N = 58-90, La_N/Sm_N = 2.09-2.66, La_N/Yb_N = 5.30-8.58) and nearly flat in the HREE region (Ho_N/Yb_N 1.01-1.48). All the considered glasses have absent or slightly positive Eu anomaly (Eu/Eu* 0.95-1.10; inset of Fig. 4). Eu/Eu* ratio decreases with increasing degree of chemical evolution with the lowest values observed in APR16-C2Bd run (see TAS diagram in Fig. 2b). Moreover, pentavalent HFSEs (i.e., Ta and Nb) are more abundant than tetravalent cations (i.e., Zr and Hf), unlike what was observed for Cpx crystals.

3.4. Partition coefficients

The clinopyroxene-melt trace element *D*-values for the reported experiments are given in Table 4.

Figure 5 shows the partition coefficients between clinopyroxene and melt for LILEs, REEs + Y, HFSEs and TEs. LILEs are incompatible (e.g., $D_{Sr} \leq 0.15$, $D_{Ba} \leq 0.05$). LREEs (e.g., $D_{La} \leq 0.20$) are always more incompatible than HREEs, which in some cases result to be compatible with cpx (e.g., D_{Tb} and D_{Dy} = 1.30-1.40 for APR16-C2Bd and APR16-C2Ad experiments). There is no clear relationship between D_i variation and dwell time for LREEs. In contrast, for MREE and HREE longest duration experiments (e.g., APR16-35 and APR16-C1Ad) are characterized by lower partition coefficients. In some cases, it was possible to note evident differences of D_i values as function of experimental time, as shown for instance by Dy behaviour in the runs at 1250 °C, where it results a compatible element in the 6 h-experiment (APR16-C1Ac; D_{Dy} = ~1) while it is moderately incompatible in the run at 9 hours (APR16-C1Ad; D_{Dy} = ~0.6). Furthermore, we observed that, except for the APR16-C3Ac run (the most hydrated run), the Eu behaves to a more incompatible extent than the adjacent REEs (i.e., Sm and Gd, Fig. 5). Given the low plagioclase abundance, this behaviour reflects only the Eu^{3+}/Eu^{2+} ratio variation caused by changing the redox conditions. As regards

HFSEs, tetravalent and pentavalent-charged cations are always incompatible (D_{Nb} and $D_{Ta} \leq 0.1$; D_{Zr} and D_{Hf} between 0.2 and 0.8), except for D_{Hf} measured in the cpx of the APR16-C2Bd run (D_{Hf} ~1.2). Finally, trace element partition coefficients of TEs (i.e., D_{Co}, D_{Cr}, D_{Ni}, D_{Sc} and D_V) range from slightly incompatible to highly compatible. In particular, D_{Co} and D_V vary between 0.7 and 3, whereas D_{Sc}, D_{Ni} and D_{Cr} are between 2 and 63.

4. Discussion

4.1. Lattice strain model (LSM)

Assuming equilibrium, the cpx/melt partition coefficient is quantitatively described by the near-parabolic relationship (Brice, 1975; Blundy and Wood, 1994; Wood and Blundy, 1997; Sun and Liang, 2012):

$$D_j^{cpx-melt} = D_0 exp\left[\frac{-4\pi E N_A}{RT}\left(\frac{r_0}{2}\left(r_0 - r_j\right)^2 - \frac{1}{3}\left(r_0 - r_j\right)^3\right)\right] \quad (1),$$

where D_0 is the clinopyroxene-melt partition coefficient for the strain-free substitution; r_0 is the optimum radius for the lattice site; r_j is the ionic radius of the element of interest in the appropriate co-ordination taken from Shannon (1976) (Table S4 in Supplementary Material 2); E is the apparent Young's modulus for the lattice site (GPa); R is the gas constant (8.3144 J mol^{-1} K^{-1}); N_A is Avogadro constant and T is temperature in K. The apparent Young's modulus E controls the tightness of the parabola, and D_0 determines the apex of the parabola with corresponding ideal lattice site r_0.

Cpx crystals are characterized by the general formula XYT_2O_6. The T site could contain tetrahedrally coordinated Si^{4+} and $^{VI}Al^{3+}$, whereas X and Y refer to two octahedral sites, a larger M2 site and a smaller M1 site (Sun, 2018). The M1 site is occupied by small cations in VI-fold coordination, including divalent Ni, Mg, Co and V, trivalent Al, Cr and Sc, tetravalent Ti, Hf and Zr, and pentavalent cations (e.g., Nb^{5+} and Ta^{5+}) (Blundy and Wood, 2003; Sun and Liang, 2012; Sun, 2018; Baziotis et al., 2019). The M2 site, instead, could host larger cations in VIII-fold coordination like

monovalent Na, K and Rb, divalent Fe, Ca, Eu, Sr, Pb and Ba, trivalent REE (La to Lu) and Y, and tetravalent U and Th (Blundy and Wood, 2003). To apply the lattice strain model (LSM) to both M1 and M2 sites and fit the experimentally determined trace element partition coefficients simultaneously we used the DOUBLE FIT program (Dalou et al., 2018), a lattice strain model fit by a differential-evolution-constrained algorithm (Storn and Price, 1997) adapted to be error weighted. When errors are large, we individually fitted the M1 and M2 sites using the SIMPLE FIT program (Dalou et al., 2018). In presence of a low number of measured trace elements, the program failed to produce good fits. Therefore, following (Dalou et al., 2018), we reduced the parameter space from the default range ($D_0^{M1\text{-}M2}$min and/or $D_0^{M1\text{-}M2}$max; $E^{M1\text{-}M2}$min and/or $E^{M1\text{-}M2}$max; $r_0^{M1\text{-}M2}$min and/or $r_0^{M1\text{-}M2}$max) to overcome this limitation. Best-fit parabolas determined for divalent, trivalent, and tetravalent cations are plotted in Figure 6 and Figure S1 in Supplementary Material 3. Fit parameters E, D_0 and r_0 for trivalent cations in M2 site are reported in Table 5, together with E and r calculated following equations from Wood and Blundy (1997):

$$r_{0(M2)}^{3+} = 0.974 + 0.067X_{Ca}^{M2} - 0.051X_{Al}^{M1}(\text{Å}) \quad (2),$$

$$E_{M2}^{3+} = 318.6 + 6.9P - 0.036T\ (GPa) \quad (3),$$

where X_{Ca}^{M2} and X_{Al}^{M1} refer to the atomic fractions of Ca and Al on the clinopyroxene M2 and M1 sites, P is in GPa and T in K. Fit parameters E, D_0 and r_0 for divalent cations in M1 and M2 site, and for trivalent and tetravalent cations in M1 site are reported in Table 5 and compared with E and r calculated using the model of Wood and Blundy (1997) for $M2^{2+}$ and that of Hill et al. (2011) for $M1^{4+}$. Following a method reported in the literature (Aigner-Torres et al., 2007; Padilla and Gualda, 2016), D_{Eu}^{3+} and D_{Eu}^{2+} were calculated using the LSM, based on the measured partition coefficients of other REE^{3+}, ideally close in ionic radius to Eu^{3+} (i.e., Gd and Sm), and Sr, respectively. These

388 data were included in the data set of divalent (D_{Eu}^{2+}) and trivalent (D_{Eu}^{3+}) cations used for the fitting.
389 For the fitting of trivalent cations in M1 site, Al in the M1 site was calculated as the difference
390 between total Al and the Al^{IV} completing the occupancy of the tetrahedral site. As regards divalent
391 cations, to understand their distribution between M1 and M2 sites, we performed a preliminary fitting
392 with DOUBLE FIT program, observing that *i*) Mn, Ca, Eu^{2+}, Sr, Pb and Ba partition only in M2 site;
393 ii) Ni partitions only in M1 site; *iii*) Mg, Co and Fe, instead, partition in both M1 and M2 sites. At
394 this point we fitted divalent cations entering only in M2 site (i.e., Mn, Ca, Eu^{2+}, Sr and ±Pb). The
395 obtained lattice strain parameters were used to calculate $D_{(Fe,Mg,Co)M2}$, that is the D value in M2 site of
396 the elements entering both the M1 and M2 sites (i.e., Fe, Mg, Co). Then, using the concentration of
397 these elements in the melt ($X_{(Fe,Mg,Co)melt}$) we calculated the concentrations of the elements in M2
398 ($X_{(Fe,Mg,Co)M2}$) and by difference in M1 ($X_{(Fe,Mg,Co)M1}$). Finally, we obtained $D_{(Fe,Mg,Co)M1}$ for these
399 elements (Table 5) dividing $X_{(Fe,Mg,Co)M1}$ with $X_{(Fe,Mg,Co)melt}$. In the fitting of the divalent cations in M1
400 site we constrained r_0 between 0.6 and 0.65 Å, based on the work of Purton et al. (1996).
401
402 *4.1.1. Onuma diagrams for divalent, trivalent and tetravalent cations*
403 The partitioning behaviour for cations (D_i) with the same valence is conveniently shown in Onuma
404 diagrams as a function of the ionic radius (Onuma et al., 1968; Leeman and Phelps, 1981; Blundy
405 and Wood, 1994), indicating which elements are compatibles/incompatibles in a given site or which
406 ones are fractionated between two distinct sites.
407 *Divalent cations.* Values of D_0, r_0 and E for divalent cations in M1 and M2 site as fitted to the
408 experimental data are given in Table 5. For divalent cations in M1 site we obtained D_0^{2+} = 6.07 ±
409 2.02, E^{2+} = 499 ± 45 GPa, and r_0^{2+} = 0.62 ± 0.01 Å (Fig. 6 and Fig. S1 in Supplementary Material 3).
410 V^{2+} was excluded from the fitting since it falls outside the parabola, probably due to its presence as
411 V^{5+}. The LSM parameters for the M2 site are D_0^{2+} = 2.50 ± 0.37, E^{2+} = 256 ± 26 GPa, and r_0^{2+} = 1.08
412 ± 0.01 Å (Fig. 6 and Fig. S1 in Supplementary Material 3). The partitioning of divalent cations into
413 M2 provides a good illustration of the control on partitioning by site size energetics. The linearized

414 regressions for Mn, Ca, Eu^{2+}, Sr and Pb produce good fits. Among these divalent cations, Ca^{2+}, that
415 dominantly occupies the M2 site in clinopyroxene (Wood and Blundy, 2001), is the cation closer to
416 the parabolas' apex and Sr is more compatible than Ba. However, the Ba position is far from the fit
417 curve of divalent cations. This anomalous behaviour is probably due to the large ionic radius that
418 produces a displacement of the nearest-neighbour ions in the charged region with an electrostatic
419 work of substitution ($\neq 0$) in spite that of Ba is a fully charge-balanced substitution in the M2 site. A
420 minor amount of melt contamination during crystal analysis can cause a large offset from the lattice
421 strain curve.
422 *Trivalent cations.* Among trivalent cations TEs (i.e., Cr and Sc) are compatible, LREEs are all
423 incompatible, while HREEs are both compatible and incompatible. Among REEs Dy and Er show
424 the highest distribution coefficients, that tend to decrease with increasing the ionic radius (towards
425 La). Because the HREEs (Dy through Lu) are more compatible than LREEs, clinopyroxene is slightly
426 enriched in HREEs. The LSM parameters for the M1 and M2 sites are D_0^{3+} = 47 ± 18 and 0.85 ±
427 0.27, E^{3+} = 1456 ± 113 and 311 ± 10 GPa, and r_0^{3+} = 0.66 ± 0.01 and 1.03 ± 0.01 Å, respectively. The
428 values of r_0^{3+} and E^{3+} in the M2 site match within the range of previous studies on basaltic
429 compositions (r_0 = 1-1.05 Å, E = 325–441 GPa; Hill et al., 2011; Dalou et al., 2012; Mollo et al.,
430 2016; Baudouin et al., 2020). Similarly, D_0^{3+} and E for the M1 site display similar values compared
431 to other basaltic compositions ones (Hill et al., 2000; Dalou et al., 2012). Figure 6 and Figure S1 in
432 Supplementary Material 3 show that our apparent partition coefficients for REEs lie on parabola-like
433 curves of Onuma diagrams (Onuma et al., 1968), similar to the trajectories found by Pappalardo et
434 al. (2008), Fedele et al. (2009) and Mollo et al. (2016) for differentiated magmas at Campi Flegrei.
435 From these diagrams, also, it is possible to note the different partitioning behaviour of Eu, which
436 occurs as both 2+ and 3+ cations, depending on fO_2. Particularly, if all Eu is present as Eu^{3+} D_{Eu} lies
437 along the parabola defined by other REE^{3+}, whereas if Eu is present as Eu^{2+}, D_{Eu} lies along the 2+
438 parabola defined by Mn, Ca, Sr, ±Pb (Aigner-Torres et al., 2007). In all the runs of this study D_{Eu} lies
439 along or close to the parabola defined by other REE^{3+}. In particular, D_{Eu} lies along the parabola in the

APR16-C3Ac run (Fig. 6c), slightly below the parabola in APR16-1C, APR16-35 and APR16-C1Ac runs (Fig. 6a, b and Fig. S1 in Supplementary Material 3), and far below the parabola in the APR16-C2Bd runs (Fig. 6d). The Eu-anomaly is due to the presence of some Eu^{2+} in the melt, which is much less compatible in the M2 site than Eu^{3+} because of its larger size (Shearer et al., 2006). Moreover, in the APR16-C2Bd run, a clear difference is observed difference between D_{Eu3+} calculated and D_{Eu} measured (Fig. 6d). The latter indeed is much lower (~0.6) than D_{Eu3+} (~1) due to the crystallization of plagioclase in this run.

The height of the parabola varies as a function of the crystal composition (Blundy and Wood, 1994, 2003) and the physical conditions of the system (Wood and Blundy, 2001; Sun and Liang, 2012). In the experimental runs the peak position can be alternatively higher or lower than 1 as a function of Al^{IV} content and temperature, in agreement with the observation that these parameters have opposing effects on trace element partitioning (Sun and Liang, 2012). For instance, we noted that the increase of Al^{IV} content, at a given temperature and under similar water content conditions, causes an increase of D_0, and a decrease of r_0 and E (Fig. 7). As a consequence, the parabolic patterns of D_{REE} move upwards and shift toward left, resulting in a more open parabola (Fig. 7a). This suggests that the increase in Al^{IV} content has a greater effect on the D_{HREE} than on $D_{LREE.}$ In fact, HREEs are more easily accommodated in clinopyroxene than LREEs (McKay et al., 1994; Lofgren et al., 2006; Mollo et al., 2013), since their smaller ionic radius can better compensate for the enlargement of the tetrahedral site induced by the replacement of Si with Al (Hill et al., 2000). Consequently, partition coefficients of HREEs, which are on the left side of the parabola, increase with the increase in Al^{IV} content, while partition coefficients of light and middle REEs (LREE and MREE), which are on the right side of the parabola, decrease slightly as the parabola shifts to the left, but increase as the parabola becomes more open, as previously observed by Sun and Liang (2012). Furthermore, even if it was not possible to discriminate the only effect of the temperature in our runs, we believe that for a constant composition an upward movement of the parabola (e.g., APR16-C3Ac and APR16-C2Ac, APR16-C1Ad and APR16-C2Bd; Fig. 7b) may be due to a decrease in temperature, following the

observations of Sun and Liang (2012). Moreover, together with tetrahedrally coordinated Al and temperature, also the undercooling ($\Delta T = T_{liquidus} - T_{experiment}$) influence the partitioning of trace element, as shown in Figure 7b. In particular, the increase of the undercooling moves the parabola upwards as observed for Al^{IV} content.

Tetravalent cations. The partition coefficients for Ti, Hf and Zr have been used to obtain E, D_0, and r_0 for the tetravalent cations. Best fits to the data yield $D_0^{4+} = 3.35 \pm 1.54$, $E^{4+} = 2600 \pm 536$ GPa, and $r_0^{4+} = 0.657 \pm 0.004$ Å (Fig. 6 and Table 5). The inferred values for E (~1950-3100 GPa) are consistent with the large values expected for small, highly charged cation sites (~800-2400 GPa; (Lundstrom et al., 1998; Hill et al., 2011; Baudouin et al., 2020). Th^{4+} and U^{4+} fall off the Ti-Hf-Zr regression suggesting that their ionic radii (1.05 and 1.00 Å, respectively) are too large for incorporation in the M1 site (Lundstrom et al., 1998). The r_0^{4+} of the M1 site is very similar to that calculated in previous studies (r_0^{4+} ~0.65-0.67 Å) (Hill et al., 2000, 2011; Mollo et al., 2016, 2018; Baudouin et al., 2020).

4.2. Influence of kinetics processes on the trace element partitioning

As general rule, partition coefficients tend to decrease with the increase of temperature (Wood and Blundy, 1997) and the effect of pressure at pressures < 2 GPa may be negligible for trace element partitioning between clinopyroxene and mafic melts (Sun and Liang, 2012; Mollo et al., 2016). As regards the influence of the chemical composition, it has been observed that in Cpx the tetrahedrally-coordinated aluminium content has a great influence on trace element partitioning (Lindstrom, 1976; Ray et al., 1983; Hart and Dunn, 1993; Forsythe et al., 1994; Lundstrom et al., 1994; Skulski et al., 1994; Lundstrom et al., 1998; Blundy et al., 1998; Hill et al., 2000; Wood and Trigila, 2001; Francis and Minarik, 2008; Sun and Liang, 2012; Yao et al., 2012; Mollo et al., 2013; Sun and Liang, 2013; Scarlato et al., 2014; Mollo et al., 2016). Nevertheless, the magnitude of the T, P and composition effects on the partitioning of trace elements between minerals and melts is not correctly assessed without considering the kinetic effect.

In the literature, the few works investigating the influence of kinetics processes on D_i values are generally focused on the effect of the cooling rates (Albarede and Bottinga, 1972; Watson, 1996; Lofgren et al., 2006; Mollo et al., 2013) and time (Arzilli et al., 2018), showing an increase of REE partition coefficients with increasing cooling rates or with decreasing crystallization times and, consequently, with increasing growth rates. Thus, since growth rates are fast at the beginning of the crystallization process and then decrease with increasing time (Vetere et al., 2013; Arzilli and Carroll, 2013; Iezzi et al., 2014; Vetere et al., 2015; Arzilli et al., 2018; Bonechi et al., 2020b, 2020a; Bonechi, 2020), we would expect a decrease of D_i values with increasing time until equilibrium conditions are reached. In this study, at static conditions (i.e., no cooling rate), D_{REE} values seem to increase with increasing time (Fig. 8), with D_{REE} values calculated in long-duration experiments higher than those calculated in short duration ones, showing thus a behaviour apparently opposite to what would have been expected. This is noticeable considering the group of runs APR16-1C/APR16-C1Ac/APR16-C2Ad (respectively 3, 6 and 9 hours long), characterized by similar T and ΔT conditions and similar Al^{IV} and H_2O contents (Table 2 and Table S2 in Supplementary Material 2). In particular, we observed an increase in D_{REE} values from 3 (APR16-1C) to 9 hours (APR16-C2Ad) experiments, more evident in the right side of the three parabolae (i.e., where the LREEs fall). Along this side, the parabolae tend to widen to the right and upwards as time increases, as confirmed by the increase of r_0 (from 1.0297 to 1.0301 Å; Table 5) and the decrease of E (from 325 to 304 GPa; Table 5) with increasing time. Conversely, there are no appreciable differences for the apical zone (where the HREEs fall) in the 3 and 6 hours experiments. This variation in the shape of the parabolae makes the effect of time on the D values stand out more clearly for the LREEs that fall on the flanks rather than for the HREEs that fall in the apical area. Indeed, D_{HREE} values of the runs at 3 and 6 hours are very similar despite their different duration, and this similarity can be explained by considering their different growth rates. Notably, the APR16-1C run (3 hours) is characterized by a growth rate ($1.6 \cdot 10^{-7}$ cm s^{-1}) higher than that of the other runs with the same duration (e.g., $3 \cdot 10^{-8}$ cm s^{-1}), as a consequence of the use of natural powder containing pre-existing nuclei as starting material, as described in the work of Bonechi

(2020). Therefore, the high growth rate of this run yields D_{REE} values higher than those expected for runs at 3 hours, but similar to those measured in the run at 6 hours (APR16-C1Ac). This agrees with observations made in previous studies (Watson, 1996; Lofgren et al., 2006), according to which, during rapid crystal growth the less efficient rejection of incompatible elements leads to higher *D*-values. Moreover, the greater similarity in D_{HREE} than in D_{LREE} in APR16-1C and APR16-C1Ac runs is due to their different diffusivities, that decrease as the REE size decreases (Zhang et al., 2010), since slow-moving elements (HREE) result more enriched compared with fast moving elements (LREE), as observed for instance during disequilibrium growth (Arzilli et al., 2018). The increase in D_{REE} values with time observed in this work, which would seem to contrast with what was observed in the literature, actually is not due to a change in time but rather to the different non-bridging oxygens per tetrahedrally co-ordinated cation ratio (NBO/T; Mysen et al., 1982, 1985) of the melts in the considered experiments, that seems to counteract the effect of increasing time which would tend to decrease the partition coefficient values. As stated in the literature, melt composition affects the melt structure, and thus trace element partition coefficients, that generally decrease with decreasing melt polymerization (i.e., increasing the NBO/T ratio) (Mysen and Virgo, 1980; Gaetani, 2004; Huang et al., 2006; Mollo et al., 2016; Michely et al., 2017), while in some cases this influence seems to be negligible in comparison to the effect of mineral chemistry (Beard et al., 2019; Baudouin et al., 2020). Indeed, as observed by Gaetani (2004), the influence of melt structure is significantly evident when NBO/T < 0.49. In this study, despite the NBO/T ratio varies between 0.6 and 1 (Table 2), we observed the influence of this parameter on REE partition coefficients. As shown in Figure 9, there is a negative correlation between D_{REE} and NBO/T ratio, described by the following equations for a representative LREE (4), MREE (5) and HREE (6) element:

$$D_{Nd} = -1.54 * \frac{NBO}{T} + 1.72 \ (R^2 = 0.98) \quad (4),$$

$$D_{Eu3+} = -2.45 * \frac{NBO}{T} + 2.73 \ (R^2 = 0.92) \quad (5),$$

$$D_{Dy} = -4.54 * \frac{NBO}{T} + 4.58 \ (R^2 = 0.99) \quad (6),$$

where R^2 is the coefficient of determination. In particular, the highest D_{REEs} are those measured in the APR16-C2Ad run characterized by the lowest NBO/T (0.70). The NBO/T ratio represents the degree of polymerization of a melt and thus yields information about its viscosity (Giordano and Dingwell, 2003). The lower NBO/T ratio of the APR16-C2Ad run with respect to that of the other two runs (0.82 and 0.78 for APR16-1C and APR16-C1Ac, respectively) suggests its higher viscosity. High viscosity values imply a lower diffusion of the elements with a consequent increase of *D* values due to the inability of diffusion to keep pace with the crystal growth rate (Lofgren et al., 2006). Moreover, the low NBO/T ratio calculated for the APR16-C2Ad run can be explained by considering its higher loss of Fe (-27 % ΔFe; Table 2) occurred during the experiment with respect to that occurred in the APR16-C1Ac and APR16-1C runs (-20 and -5 % ΔFe, respectively; Table 2). This difference, that suggests a different melt viscosity between the runs, highlights the strong influence of this latter parameter on the partitioning of trace elements between cpx and basaltic melt.

4.3 Deep differentiation of primitive parental K-basaltic magmas of the CFVD

The partitioning of trace elements between crystals and melts provides an important petrogenetic tool for understanding magmatic processes. Trace elements in volcanic rocks tend to fractionate into specific minerals and therefore are useful in formulating models for magmatic differentiation. Nevertheless, phenocrysts formed in deeper magmatic reservoirs are frequently cannibalized during their ascent in the plumbing system (e.g., Tecchiato et al., 2018b, 2018a). Our study shows that the mineral assemblage obtained from high pressure experiments is similar to that obtained from mafic volcanic products of Campi Flegrei (Table 2). This petrological evidence allows us to validate

567 geochemical models. In the Campi Flegrei Volcanic District mafic products (shoshonitic basalts,
568 trachybasalts, basanites and tephrites) are poorly represented with respect to the differentiated
569 compositions (trachyte or phonolite) that are the largest part of the magma volume erupted (several
570 hundreds of cubic kilometers; e.g., Orsi et al., 1992; Fedele et al., 2003). This suggested that a huge
571 volume of magmas should be differentiated by ponding at variable depths within the crust, producing
572 cumulates joint to the most evolved magmas that have fed the volcanism of the Campania Plain over
573 the past ca. 1.8 Ma (Fedi et al., 2018 and references therein). A first step of differentiation has been
574 supposed at upper mantle-crustal boundary (i.e., at the Moho = ~25 km of depth; Di Stefano et al.,
575 2011) on the basis of the results of melt inclusion studies (Mormone et al., 2011; Moretti et al., 2013),
576 seismic data interpretations (Di Stefano et al., 1999; Piochi et al., 2005; Chiarabba et al., 2008) and
577 gravimetric and petrological modelling (Fedi et al., 2018). As shown in Perinelli et al. (2019), a stage
578 of high-pressure crystallization is also revealed by the estimate of *T-P* crystallization conditions of
579 clinopyroxenes phenocrysts from the less differentiated CFVD products indicating crystallization
580 temperatures and pressures between 1140 and 1220 °C and between 0.6 and 0.9 GPa, respectively.
581 Fedi et al. (2018) combining gravimetric data with petrological modelling suggest that a first step of
582 differentiation of the Campi Flegrei primary magmas may occur as a result of the underplating at the
583 Moho level. In this deep reservoir K-trachybasalt melts could be originated after about 30 wt%
584 fractionation of gabbrous cumulates. On the other hand, our experimental results along with those
585 reported in Perinelli et al. (2019) indicate that at pressure corresponding to the Moho depth
586 plagioclase has a limited role in the differentiation of K-trachybasalts from parental APR16-like
587 magmas. Indeed, residual melts of trachybasalt can formed after the fractionation of 20-30% of a
588 clinopyroxenitic mineral assemblage (Table 2 of this study and Table 2 in Perinelli et al., 2019) in a
589 range of temperature that depending on water content (1 up to 3 wt%), varies from 1250 and 1150
590 °C. To examine the role of plagioclase in the deep differentiation process of a primitive parental K-
591 basaltic magma we calculated the concentration of selected elements in residual trachybasaltic melts
592 due to crystal-liquid fractionation process (FC). To model the FC process, we used the Excel©

593 spreadsheet program “FC-AFC-FCA and mixing modeler” (Ersoy and Helvaci, 2010) considering:
594 1) the partition coefficients clinopyroxene/melt determined in this study from the longest experiments
595 for which clinopyroxene is in equilibrium with the residual melt (Table S2 in Supplementary Material
596 2) and 2) a fractionate mineral assemblage formed by clinopyroxene + olivine ± plagioclase (Fig. 9).
597 Modelling results indicate that significant amounts of plagioclase crystallization (>10 wt%) did not
598 fully reproduce the composition of CFVD trachybasalts, particularly for the HREEs (Fig. S2 in
599 Supplementary Material 3). The latter increase also using the highest HREE partition coefficients
600 between clinopyroxene and glass obtained in the longest or hydrated experiments (i.e., APR16-C2Bd
601 and APR16-C3Ac, Table 2 and Table 4). Particularly, by increasing the percentage of plagioclase in
602 the fractionated solid, a slight increase in incompatible elements is observed, including the HREEs.
603 Moreover, it is clearly seen that the increase in plagioclase fails to model the Sr abundances. This is
604 a key aspect since Sr is compatible in plagioclase and compatibles elements are much more sensitive
605 than incompatible ones to low degrees of fractionation. On the contrary, the fractionation of 15-26
606 wt% of clinopyroxene + 2-6 wt% of olivine, corresponding to results of the crystallization
607 experiments in which the residual melts had a trachybasalt composition (Table 2 of this study and
608 Table 2 in Perinelli et al., 2019), well mimics the trace element pattern of natural trachybasalts (Fig.
609 9).
610
611 **5. Conclusions**
612 This study provides new experimental data on trace element partition coefficients between
613 clinopyroxene and a K-basaltic melt, showing the influence of temperature, chemical composition
614 and also kinetic effects like growth rate and order-disorder crystal growth. Particularly, the rapid
615 growth of clinopyroxene under disequilibrium conditions and/or in presence of pre-existing nuclei
616 under near-equilibrium conditions causes less efficient rejection of incompatible elements (e.g.,
617 REEs), since disordered crystal growth is the preferred process during the crystallization, yielding
618 higher D_{REE} than those calculated in presence of lower growth rates, generally under equilibrium

conditions. Since growth rates are fast at the beginning of the crystallization process and then decrease with increasing time, D_i values should decrease with increasing time. Therefore, the increase in D_{REE} values with time observed in some runs of this work is not related to a change in time but rather to the different NBO/T ratio. The low NBO/T ratio calculated in the run with longer duration (9 hours) is linked to its higher loss of Fe with respect to the other run at 3 and 6 hours, pointing out the strong influence of melt structure and thus of melt viscosity on the partitioning behaviour of trace elements between cpx and basaltic melt. Finally, by using the partition coefficients clinopyroxene/melt determined in this study, geochemical data modelling applied to natural less evolved products of Campi Flegrei Volcanic District, indicate that the differentiation process at mantle-crustal boundary depth is controlled by fractionation of clinopyroxene >> olivine mineral assemblage and that K-trachybasalts can derive from parental APR16-like magmas after the fractionation of about 20-30% of a clinopyroxenitic cumulate.

Acknowledgments

We are very grateful to Dr. Fabio Arzilli, an anonymous reviewer and the Associate Editor Wim van Westrenen for their helpful and constructive comments on an early version of the manuscript.

We thank Luca Ziberna (BGI Bayreuth) for preparing APR16GL sample. We thank M. Albano and M. Serracino (CNR-IGAG), R. Jedlicka and M. Racek (Institute of Petrology and Structural Geology, Charles University of Prague) for assistance during SEM and EPMA analytical sessions.

Funding

This research has been conducted with the financial support of the HP-HT Laboratory at the Department of Earth Sciences of Sapienza - University of Rome and with the financial support of the project M_011177_14_D_MAGRI_10-MIUR funded to B.B.

References

Aigner-Torres M., Blundy J., Ulmer P. and Pettke T. (2007) Laser Ablation ICPMS study of trace element partitioning between plagioclase and basaltic melts: An experimental approach. *Contrib. Mineral. Petrol*. **153**, 647–667.

Albarede F. and Bottinga Y. (1972) Kinetic disequilibrium in trace element partitioning between phenocrysts and host lava. *Geochim. Cosmochim. Acta* **36**, 141–156.

Anders E. and Grevesse N. (1989) Abundances of the elements: Meteoritic and solar. *Geochim. Cosmochim. Acta* **53**, 197–214.

Arzilli F. and Carroll M. R. (2013) Crystallization kinetics of alkali feldspars in cooling and decompression-induced crystallization experiments in trachytic melt. *Contrib. Mineral. Petrol*. **166**, 1011–1027.

Arzilli F., Fabbrizio A., Schmidt M. W., Petrelli M., Maimaiti M., Dingwell D. B., Paris E., Burton M. and Carroll M. R. (2018) The effect of diffusive re-equilibration time on trace element partitioning between alkali feldspar and trachytic melts. *Chem. Geol*. **495**, 50–66.

Asimow P. and Ghiorso M. S. (1998) Algorithmic modifications extending MELTS to calculate subsolidus phase relations. *Am. Mineral*. **83**, 1127–1132.

De Astis G., Pappalardo L. and Piochi M. (2004) Procida volcanic history: New insights into the evolution of the Phlegraean Volcanic District (Campania region, Italy). *Bull. Volcanol*. **66**, 622–641.

Baudouin C., France L., Boulanger M., Dalou C. and Devidal J. (2020) Trace element partitioning between clinopyroxene and alkaline magmas: parametrization and role of M1 site on HREE enrichment in clinopyroxenes. *Contrib. Mineral. Petrol*. **175**, 42.

Baziotis I., Xydous S., Asimow P. D., Mavrogonatos C., Flemetakis S., Klemme S. and Berndt J. (2019) The potential of phosphorus in clinopyroxene as a geospeedometer: Examples from mantle xenoliths. *Geochim. Cosmochim. Acta* **266**, 307–331.

Beard C. D., Van Hinsberg V. J., Stix J. and Wilke M. (2019) Clinopyroxene/Melt Trace Element Partitioning in Sodic Alkaline Magmas. *J. Petrol*. **60**, 1797–1823.

Beattie P., Drake M., Jones J., Leeman W., Longhi J, McKay G., Nielsen R., Palme H., Shaw D., Takahashi E. and Watson E.B. (1993). Terminology for trace element partitioning. *Geochim. Cosmochim. Acta* **57**, 1605-1606.

Bédard J. H. (2010) Parameterization of the Fe=Mg exchange coefficient (Kd) between clinopyroxene and silicate melts. *Chem. Geol*. **274**, 169–176.

Bédard J. H. (2014) Parameterizations of calcic clinopyroxene - Melt trace element partition coefficients. *Geochem. Geophys. Geosyst*. **15**, 303–336.

Bennett S. L., Blundy J. and Elliott T. (2004) The effect of sodium and titanium on crystal-melt partitioning of trace elements. *Geochim. Cosmochim. Acta* **68**, 2335–2347.

Blundy J. D., Robinson J. A. C. and Wood B. J. (1998) Heavy REE are compatible in clinopyroxene on the spinel lherzolite solidus. *Earth Planet. Sci. Lett*. **160**, 493–504.

Blundy J. D. and Wood B. J. (1991) Crystal-chemical controls on the partitioning of Sr and Ba between plagioclase feldspar, silicate melts, and hydrothermal solutions. *Geochim. Cosmochim. Acta* **55**, 193–209.

Blundy J. D. and Wood B. J. (2003) Partitioning of trace elements between crystals and melts. *Earth Planet. Sci. Lett*. **210**, 383–397.

Blundy J. D. and Wood B. J. (1994) Prediction of crystal-melt partition coefficients from elastic moduli. *Nature* **372**, 452–454.

Bohlen, S. R., Essene, E. J. and Boettcher, A. L. (1980) Reinvestigation and application of olivine-quartz-orthopyroxene barometry. *Earth Planet. Sci. Lett*. ***47***, 1-10.

Bonechi B. (2020) Influence of Pre-Existing Nuclei on the Crystallization Kinetics of Primitive Alkaline Magmas: Insights on the Deep Feeding System of the Campi Flegrei Volcanic District. *Minerals* **10**, 234.

695 Bonechi B., Perinelli C. and Gaeta M. (2020a) Clinopyroxene growth rates at high pressure:
696 constraints on magma recharge of the deep reservoir of the Campi Flegrei Volcanic District (south
697 Italy). *Bull. Volcanol*. **82**, 5.
698 Bonechi B., Perinelli C., Gaeta M., Tecchiato V. and Fabbrizio A. (2020b) Amphibole growth from
699 a primitive alkaline basalt at 0.8 GPa: time-dependent compositional evolution, growth rate and
700 competition with clinopyroxene. *Lithos* **354–355**, 105272.
701 Brice J. C. (1975) Some thermodynamic aspects of the growth of strained crystals. *J. Cryst. Growth*
702 **28**, 249–253.
703 Cartier C., Hammouda T., Doucelance R., Boyet M., Devidal J. L. and Moine B. (2014) Experimental
704 study of trace element partitioning between enstatite and melt in enstatite chondrites at low oxygen
705 fugacities and 5 GPa. *Geochim. Cosmochim. Acta* **130**, 167–187.
706 Chen Y. and Zhang Y. (2009) Clinopyroxene dissolution in basaltic melt. *Geochim. Cosmochim. Acta*
707 **73**, 5730–5747.
708 Chiarabba C., De Gori P. and Speranza F. (2008) The southern Tyrrhenian subduction zone: Deep
709 geometry, magmatism and Plio-Pleistocene evolution. *Earth Planet. Sci. Lett*. **268**, 408–423.
710 Colson R. O., McKay G. A. and Taylor L. A. (1988) Temperature and composition dependencies of
711 trace element partitioning: Olivine/melt and low-Ca pyroxene/melt. *Geochim. Cosmochim. Acta* **52**,
712 539–553.
713 Conte A. M., Dolfi D., Gaeta M., Misiti V., Mollo S. and Perinelli C. (2009) Experimental constraints
714 on evolution of leucite-basanite magma at 1 and 10^{-4} GPa: implications for parental compositions of
715 Roman high-potassium magmas. *Eur. J. Mineral*. **21**, 763–782.
716 D'Antonio M., Civetta L. and Di Girolamo P. (1999) Mantle source heterogeneity in the Campanian
717 Region (South Italy) as inferred from geochemical and isotopic features of mafic volcanic rocks with
718 shoshonitic affinity. *Mineral. Petrol*. **67**, 163–192.
719 Dalou C., Boulon J., T. Koga K., Dalou R. and Dennen R. L. (2018) DOUBLE FIT: Optimization
720 procedure applied to lattice strain model. *Comput. Geosci*. **117**, 49–56.

721 Dalou C., Koga K. T., Shimizu N., Boulon J. and Devidal J. L. (2012) Experimental determination
722 of F and Cl partitioning between lherzolite and basaltic melt. *Contrib. Mineral. Petrol*. **163**, 591–609.
723 Devine J. D., Gardner J. E., Brack H. P., Layne G. D. and Rutherford M. J. (1995) Comparison of
724 microanalytical methods for estimating H_2O contents of silicic volcanic glasses. *Am. Mineral*. **80**,
725 319–328.
726 Drexler J. W., Bornhorst T. J. and Noble D. C. (1983) Trace-element sanidine/glass distribution
727 coefficients for peralkaline silicic rocks and their implications to peralkaline petrogenesis. *Lithos* **16**,
728 265–271.
729 Dygert N., Draper D. S., Rapp J. F., Lapen T. J., Fagan A. L. and Neal C. R. (2020) Experimental
730 determinations of trace element partitioning between plagioclase, pigeonite, olivine, and lunar
731 basaltic melts and an fO_2 dependent model for plagioclase-melt Eu partitioning. *Geochim.*
732 *Cosmochim. Acta* **279**, 258–280.
733 Ersoy Y. and Helvaci C. (2010) FC-AFC-FCA and mixing modeler: A Microsoft® Excel©
734 spreadsheet program for modeling geochemical differentiation of magma by crystal fractionation,
735 crustal assimilation and mixing. *Comput. Geosci*. **36**, 383–390.
736 Fedele F. G., Giaccio B., Isaia R. and Orsi G. (2003) The Campanian ignimbrite eruption, Heinrich
737 event 4, and palaeolithic change in Europe: A high-resolution investigation. In Geophysical
738 Monograph Series pp. 301–325.
739 Fedele L., Zanetti A., Morra V., Lustrino M., Melluso L. and Vannucci R. (2009)
740 Clinopyroxene/liquid trace element partitioning in natural trachyte - Trachyphonolite systems:
741 Insights from Campi Flegrei (southern Italy). *Contrib. Mineral. Petrol*. **158**, 337–356.
742 Fedi M., Cella F., D'Antonio M., Florio G., Paoletti V. and Morra V. (2018) Gravity modeling finds
743 a large magma body in the deep crust below the Gulf of Naples, Italy. *Sci. Rep*. **8**, 1–19.
744 Forsythe L., Nielsen R. and Fisk M. R. (1994) High-field-strength element partitioning between
745 pyroxene and basaltic to dacitic magmas. *Chem. Geol*. **117**, 107–125.

746 Francis D. and Minarik W. (2008) Aluminum-dependent trace element partitioning in clinopyroxene.
747 *Contrib. Mineral. Petrol*. **156**, 439–451.
748 Freda C., Baker D. R. and Ottolin L. (2001) Reduction of water loss from gold-palladium capsules
749 during piston-cylinder experiments by use of pyrophyllite powder. *Am. Mineral*. **86**, 234–237.
750 Gaetani G. A. (2004) The influence of melt structure on trace element partitioning near the peridotite
751 solidus. *Contrib. Mineral. Petrol*. **147**, 511–527.
752 Gallahan W. and Nielsen R. (1992) The partitioning of Sc, Y, and the rare earth elements between
753 high-Ca pyroxene and natural mafic to intermediate lavas at 1 atmosphere. *Geochim. Cosmochim.*
754 *Acta* **56**, 2387–2404.
755 Ghiorso M. S. and Sack R. O. (1995) Chemical mass transfer in magmatic processes IV. A revised
756 and internally consistent thermodynamic model for the interpolation and extrapolation of liquid-solid
757 equilibria in magmatic systems at elevated temperatures and pressures. *Contrib. Mineral. Petrol*. **119**,
758 197–212.
759 Giordano D. and Dingwell D. B. (2003) Non-Arrhenian multicomponent melt viscosity: A model.
760 *Earth Planet. Sci. Lett*. **208**, 337–349.
761 Green T. H. and Pearson N. J. (1983) Effect of pressure on rare earth element partition coefficients
762 in common magmas. *Nature* **305**, 414–416.
763 Green T. H. and Pearson N. J. (1985) Rare earth element partitioning between clinopyroxene and
764 silicate liquid at moderate to high pressure. *Contrib. Mineral. Petrol*. **91**, 24–36.
765 Hart S. R. and Dunn T. (1993) Experimental Cpx Melt Partitioning of 24 Trace-Elements. *Contrib.*
766 *Mineral. Petrol*. **113**, 1–8.
767 Henderson C. M. B. and Pierozynski W. J. (2012) An experimental study of Sr, Ba and Rb partitioning
768 between alkali feldspar and silicate liquid in the system nepheline-kalsilite-quartz at 0.1 GPa $P_{(H2O)}$:
769 a revisitation and reassessment. *Mineral. Mag*. **76**, 157–190.
770 Higuchi H. and Nagasawa H. (1969) Partition of trace elements between rock-forming minerals and
771 the host volcanic rocks. *Earth Planet. Sci. Lett*. **7**, 281–287.

772 Hill E., Blundy J. D. and Wood B. J. (2011) Clinopyroxene-melt trace element partitioning and the
773 development of a predictive model for HFSE and Sc. *Contrib. Mineral. Petrol*. **161**, 423–438.
774 Hill E., Wood B. J. and Blundy J. D. (2000) The effect of Ca-Tschermaks component on trace element
775 partitioning between clinopyroxene and silicate melt. *Lithos* **53**, 203–215.
776 Huang F., Lundstrom C. C. and McDonough W. F. (2006) Effect of melt structure on trace-element
777 partitioning between clinopyroxene and silicic, alkaline, aluminous melts. *Am. Mineral*. **91**, 1385–
778 1400.
779 Hughes E. C., Buse B., Kearns S. L., Blundy J. D., Kilgour G. N. and Mader H. M. (2019) Low
780 analytical totals in EPMA of hydrous silicate glass due to sub-surface charging: Obtaining accurate
781 volatiles by difference. *Chem. Geol*. **505**, 48–56.
782 Humphreys M. C. S., Kearns S. L. and Blundy J. D. (2006) SIMS investigation of electron-beam
783 damage to hydrous, rhyolitic glasses: implications for melt inclusion analysis. *Am. Mineral*. **91**, 667–
784 679.
785 Iezzi G., Mollo S., Shahini E., Cavallo A. and Scarlato P. (2014) The cooling kinetics of plagioclase
786 feldspar as revealed by electron-microprobe mapping. *Am. Mineral*. **99**, 898–907.
787 Johannes W., Bell P. M., Mao H. K., Boettcher A. L., Chipman D. W., Hays J. F., Newton R. C. and
788 Seifert F. (1971) An interlaboratory comparison of piston-cylinder pressure calibration using the
789 albite-breakdown reaction. *Contrib. Mineral. Petrol*. **32**, 24–38.
790 Jones J. H. (1995) Experimental trace element partitioning. In Rock physics and phase relations: A
791 handbook of physical constants pp. 73–104.
792 Kress V. C. and Carmichael I. S. E. (1991) The compressibility of silicate liquids containing Fe_2O_3
793 and the effect of composition, temperature, oxygen fugacity and pressure on their redox states.
794 *Contrib. Mineral. Petrol*. **108**, 82–92.
795 Leeman W. P. and Phelps D. W. (1981) Partitioning of rare earths and other trace elements between
796 sanidine and coexisting volcanic glass. *J. Geophys. Res*. **86**, 10193–10199.

797 Lindstrom D. (1976) Partitioning of ferric iron between diopside and silicate liquid. Eos, *Trans. Am.*
798 *Geophys. Union* **57**, 339–339.
799 Lofgren G. E., Huss G. R. and Wasserburg G. J. (2006) An experimental study of trace-element
800 partitioning between Ti-Al-clinopyroxene and melt: Equilibrium and kinetic effects including sector
801 zoning. *Am. Mineral*. **91**, 1596–1606.
802 Lundstrom C. C., Shaw H. F., Ryerson F. J., Phinney D. L., Gill J. B. and Williams Q. (1994)
803 Compositional controls on the partitioning of U, Th, Ba, Pb, Sr and Zr between clinopyroxene and
804 haplobasaltic melts: implications for uranium series disequilibria in basalts. *Earth Planet. Sci. Lett*.
805 **128**, 407–423.
806 Lundstrom C. C., Shaw H. F., Ryerson F. J., Williams Q. and Gill J. (1998) Crystal chemical control
807 of clinopyroxene-melt partitioning in the Di-Ab-An system: Implications for elemental fractionations
808 in the depleted mantle. *Geochim. Cosmochim. Acta* **62**, 2849–2862.
809 Mahood G. and Hildreth W. (1983) Large partition coefficients for trace elements in high-silica
810 rhyolites. *Geochim. Cosmochim. Acta* **47**, 11–30.
811 Le Maitre R., Streckeisen A., Zanettin B. and Bas M. (2002) Igneous rocks: a classification and
812 glossary of terms: recommendations of the International Union of Geological Sciences
813 Subcommission on the Systematics., Cambridge University Press.
814 Mazzeo F. C., D'Antonio M., Arienzo I., Aulinas M., Di Renzo V. and Gimeno D. (2014) Subduction-
815 related enrichment of the Neapolitan volcanoes (Southern Italy) mantle source: New constraints on
816 the characteristics of the slab-derived components. *Chem. Geol*. **386**, 165–183.
817 McDade P., Blundy J. D. and Wood B. J. (2003) Trace element partitioning on the Tinaquillo solidus
818 at 1.5 GPa. *Phys. Earth Planet. Inter*. **139**, 129–147.
819 McDonough W. F. and Sun S. s. (1995) The composition of the Earth. *Chem. Geol*. **120**, 223–253.
820 McKay G., Le L., Wagstaff J. and Crozaz G. (1994) Experimental partitioning of rare earth elements
821 and strontium: Constraints on petrogenesis and redox conditions during crystallization of Antarctic
822 angrite Lewis Cliff 86010. *Geochim. Cosmochim. Acta* **58**, 2911–2919.

823 Michely L. T., Leitzke F. P., Speelmanns I. M. and Fonseca R. O. C. (2017) Competing effects of
824 crystal chemistry and silicate melt composition on trace element behavior in magmatic systems:
825 insights from crystal/silicate melt partitioning of the REE, HFSE, Sn, In, Ga, Ba, Pt and Rh. *Contrib.*
826 *Mineral. Petrol*. **172**, 39.
827 Milman-Barris M. S., Beckett J. R., Baker M. B., Hofmann A. E., Morgan Z., Crowley M. R.,
828 Vielzeuf D. and Stolper E. (2008) Zoning of phosphorus in igneous olivine. *Contrib. Mineral. Petrol.*
829 **155**, 739–765.
830 Mollo S., Blundy J. D., Iezzi G., Scarlato P. and Langone A. (2013) The partitioning of trace elements
831 between clinopyroxene and trachybasaltic melt during rapid cooling and crystal growth. *Contrib.*
832 *Mineral. Petrol*. **166**, 1633–1654.
833 Mollo S., Blundy J., Scarlato P., De Cristofaro S. P., Tecchiato V., Di Stefano F., Vetere F., Holtz F.
834 and Bachmann O. (2018) An integrated P-T-H_2O-lattice strain model to quantify the role of
835 clinopyroxene fractionation on REE+Y and HFSE patterns of mafic alkaline magmas: Application to
836 eruptions at Mt. Etna. *Earth-Sci Rev*. **185**, 32–56.
837 Mollo S., Forni F., Bachmann O., Blundy J. D., De Astis G. and Scarlato P. (2016) Trace element
838 partitioning between clinopyroxene and trachy-phonolitic melts: A case study from the Campanian
839 Ignimbrite (Campi Flegrei, Italy). *Lithos* **252–253**, 160–172.
840 Mollo S., Putirka K., Iezzi G., Del Gaudio P. and Scarlato P. (2011) Plagioclase-melt (dis)equilibrium
841 due to cooling dynamics: Implications for thermometry, barometry and hygrometry. *Lithos* **125**, 221–
842 235.
843 Morabito S., Petrosino P., Milia A., Sprovieri M. and Tamburrino S. (2014) A multidisciplinary
844 approach for reconstructing the stratigraphic framework of the last 40 ka in a bathyal area of the
845 eastern Tyrrhenian Sea. *Glob. Planet. Change* **123**, 121–138.
846 Moretti R., Arienzo I., Orsi G., Civetta L. and D'antonio M. (2013) The deep plumbing system of
847 ischia: A physico-chemical window on the fluid-saturated and CO_2-sustained neapolitan volcanism
848 (southern Italy). *J. Petrol*. **54**, 951–984.

849 Morgan VI. G. B. and London D. (2003) Trace-element partitioning at conditions far from
850 equilibrium: Ba and Cs distributions between alkali feldspar and undercooled hydrous granitic liquid
851 at 200 MPa. *Contrib. Mineral. Petrol*. **144**, 722–738.
852 Morgan VI G. B. and London D. (1996) Optimizing the electron microprobe analysis of hydrous
853 alkali aluminosilicate glasses. *Am. Mineral*. **81**, 1176–1185.
854 Morimoto N., Fabries J., Ferguson A. K., Ginzburg I. V., Ross M., Seifert F. A., J. Z., Aoki K. and
855 Gottardi G. (1998) Nomenclature of pyroxenes Subcommittee. *Am. Mineral*. **73**, 1123–1133.
856 Mormone A., Piochi M., Bellatreccia F., De Astis G., Moretti R., Ventura G. Della, Cavallo A. and
857 Mangiacapra A. (2011) A CO_2-rich magma source beneath the Phlegraean Volcanic District
858 (Southern Italy): Evidence from a melt inclusion study. *Chem. Geol*. **287**, 66–80.
859 Mysen B. O. and Virgo D. (1980) Trace element partitioning and melt structure: An experimental
860 study at 1 atm pressure. *Geochim. Cosmochim. Acta* **44**, 1917–1930.
861 Mysen B. O., Virgo D. and Seifert F. A. (1985) Relationships between properties and structure of
862 aluminosilicate melts. *Am. Mineral*. **70**, 88–105.
863 Mysen B. O., Virgo D. and Seifert F. A. (1982) The structure of silicate melts: Implications for
864 chemical and physical properties of natural magma. *Rev. Geophys*. 20, 353–383.
865 Nielsen R. L. (1985) A method for the elimination of the compositional dependence of trace element
866 distribution coefficients. *Geochim. Cosmochim. Acta* **49**, 1775–1779.
867 Onuma N., Higuchi H., Wakita H. and Nagasawa H. (1968) Trace element partition between two
868 pyroxenes and the host lava. *Earth Planet. Sci. Lett*. **5**, 47–51.
869 Orsi G., D'Antonio M., Vita S. de and Gallo G. (1992) The Neapolitan Yellow Tuff, a large-
870 magnitude trachytic PhreatoPlinian eruption: eruptive dynamics, magma withdrawal and caldera
871 collapse. *J. Volcanol. Geotherm. Res*. **53**, 275–287.
872 Padilla A. J. and Gualda G. A. R. (2016) Crystal-melt elemental partitioning in silicic magmatic
873 systems: An example from the Peach Spring Tuff high-silica rhyolite, Southwest USA. *Chem. Geol.*
874 **440**, 326–344.

875 Pappalardo L., Civetta L., D'Antonio M., Deino A., Di Vito M., Orsi G., Carandente A., de Vita S.,
876 Isaia R. and Piochi M. (1999) Chemical and Sr-isotopical evolution of the Phlegraean magmatic
877 system before the Campanian Ignimbrite and the Neapolitan Yellow Tuff eruptions. *J. Volcanol.*
878 *Geotherm. Res*. **91**, 141–166.
879 Pappalardo L., Ottolini L. and Mastrolorenzo G. (2008) The Campanian Ignimbrite (southern Italy)
880 geochemical zoning: Insight on the generation of a super-eruption from catastrophic differentiation
881 and fast withdrawal. *Contrib. Mineral. Petrol*. **156**, 1–26.
882 Pearce N. J. G., Perkins W. T., Westgate J. A., Gorton M. P., Jackson S. E., Neal C. R. and Chenery
883 S. P. (1997) A compilation of new and published major and trace element data for NIST SRM 610
884 and NIST SRM 612 glass reference materials. *Geostand. Newsl*. **21**, 115–144.
885 Perinelli C., Gaeta M., Bonechi B., Granati S. F., Freda C., D'Antonio M., Stagno V., Sicola S. and
886 Romano C. (2019) Effect of water on the phase relations of primitive K-basalts: Implications for
887 high-pressure differentiation in the Phlegraean Volcanic District magmatic system. *Lithos* **342–343**,
888 530–541.
889 Petrelli M., Caricchi L. and Ulmer P. (2007) Application of high spatial resolution laser ablation ICP-
890 MS to crystal-melt trace element partition coefficient determination. *Geostand. Geoanalytical Res*.
891 **31**, 13–25.
892 Petrelli M., Laeger K. and Perugini D. (2016) High spatial resolution trace element determination of
893 geological samples by laser ablation quadrupole plasma mass spectrometry: implications for glass
894 analysis in volcanic products. *Geosci. J.* **20**, 851–863.
895 Petrelli M., Perugini D., Alagna K. E., Poli G. and Peccerillo A. (2008) Spatially resolved and bulk
896 trace element analysis by laser ablation - Inductively coupled plasma - Mass spectrometry (LA-ICP-
897 MS). *Period. Mineral*. **77**, 3–21.
898 Philpotts J. A. and Schnetzler C. C. (1970) Phenocryst-matrix partition coefficients for K, Rb, Sr and
899 Ba, with applications to anorthosite and basalt genesis. *Geochim. Cosmochim. Acta* **34**, 307–322.

900 Piochi M., Mastrolorenzo G. and Pappalardo L. (2005) Magma ascent and eruptive processes from
901 textural and compositional features of Monte Nuovo pyroclastic products, Campi Flegrei, Italy. *Bull.*
902 *Volcanol*. **67**, 663–678.
903 Presnall D. C., Dixon S. A., Dixon J. R., O'Donnell T. H., Brenner N. L., Schrock R. L. and Dycus
904 D. W. (1978) Liquidus phase relations on the join diopside-forsterite-anorthite from 1 atm to 20 kbar:
905 Their bearing on the generation and crystallization of basaltic magma. *Contrib. Mineral. Petrol*. **66**,
906 203–220.
907 Purton J. A., Allan N. L., Blundy J. D. and Wasserman E. A. (1996) Isovalent trace element
908 partitioning between minerals and melts: A computer simulation study. *Geochim. Cosmochim. Acta*
909 **60**, 4977–4987.
910 Putirka K. D. (2008) Thermometers and Barometers for Volcanic Systems. In Minerals, Inclusions
911 And Volcanic Processes (eds. K. D. Putirka and F. J. Tepley III). Reviews in Mineralogy and
912 Geochemistry. pp. 61–120.
913 Ray G. L., Shimizu N. and Hart S. R. (1983) An ion microprobe study of the partitioning of trace
914 elements between clinopyroxene and liquid in the system diopside-albite-anorthite. *Geochim.*
915 *Cosmochim. Acta* **47**, 2131–2140.
916 Scarlato P., Mollo S., Blundy J. D., Iezzi G. and Tiepolo M. (2014) The role of natural solidification
917 paths on REE partitioning between clinopyroxene and melt. *Bull. Volcanol*. **76**, 1–4.
918 Schnetzler C. C. and Philpotts J. A. (1970) Partition coefficients of rare-earth elements between
919 igneous matrix material and rock-forming mineral phenocrysts-II. *Geochim. Cosmochim. Acta* **34**,
920 331–340.
921 Shannon B. Y. R. D. (1976) Revised Effective Ionic Radii and Systematic Studies of Interatomie
922 Distances in Halides and Chaleogenides. *Acta Crystallogr*. **A32**, 751.
923 Shea T., Hammer J. E., Hellebrand E., Mourey A. J., Costa F., First E. C., Lynn K. J. and Melnik O.
924 (2019) Phosphorus and aluminum zoning in olivine: contrasting behavior of two nominally
925 incompatible trace elements. *Contrib. Mineral. Petrol*. **174**, 85.

926 Shearer C. K., Papike J. J. and Karner J. M. (2006) Pyroxene europium valence oxybarometer: Effects
927 of pyroxene composition, melt composition, and crystallization kinetics. *Am. Mineral*. **91**, 1565–
928 1573.
929 Shimizu N. (1974) An experimental study of the partitioning of K, Rb, Cs, Sr and Ba between
930 clinopyroxene and liquid at high pressures. *Geochim. Cosmochim. Acta* **38**, 1789–1798.
931 Shimizu N. (1981) Trace element incorporation into growing augite phenocryst. *Nature* **289**, 575–
932 577.
933 Skála R., Strnad L., McCammon C. and Čada M. (2009) Moldavites from the Cheb Basin, Czech
934 Republic. *Geochim. Cosmochim. Acta* **73**, 1145–1179.
935 Skulski T., Minarik W. and Watson E. B. (1994) High-pressure experimental trace-element
936 partitioning between clinopyroxene and basaltic melts. *Chem. Geol*. **117**, 127–147.
937 Di Stefano R., Bianchi I., Ciaccio M. G., Carrara G. and Kissling E. (2011) Three-dimensional Moho
938 topography in Italy: New constraints from receiver functions and controlled source seismology.
939 *Geochem. Geophys. Geosyst*. **12**, 1–15.
940 Di Stefano R., Chiarabba C., Lucente F. and Amato A. (1999) Crustal and uppermost mantle structure
941 in Italy. *Geophys. J. Int.* **139**, 438–498.
942 Storn R. and Price K. (1997) Differential Evolution - A Simple and Efficient Heuristic for Global
943 Optimization over Continuous Spaces. *J. Glob. Optim*. **11**, 341–359.
944 Strnad L., Mihaljevic M. and Sebek O. (2005) Laser Ablation and Solution ICP-MS Determination
945 of Rare Earth Elements in USGS BIR-1G, BHVO-2G and BCR-2G Glass Reference Materials.
946 *Geostand. Geoanalytical Res*. **29**, 303–314.
947 Sun C. (2018) Partitioning and Partition Coefficients. In Encyclopedia of Geochemistry
948 Sun C. and Liang Y. (2012) Distribution of REE between clinopyroxene and basaltic melt along a
949 mantle adiabat: Effects of major element composition, water, and temperature. *Contrib. Mineral.*
950 *Petrol.* **163**, 807–823.

951 Tecchiato V., Gaeta M., Mollo S., Bachmann O., Quadt A. Von and Scarlato P. (2018a) Snapshots
952 of primitive arc magma evolution recorded by clinopyroxene textural and compositional variations:
953 The case of hybrid crystal-rich enclaves from Capo Marargiu Volcanic District (Sardinia, Italy). *Am.*
954 *Mineral. J. Earth Planet. Mater*. **103**, 899–910.
955 Tecchiato V., Gaeta M., Mollo S., Scarlato P., Bachmann O. and Perinelli C. (2018b) Petrological
956 constraints on the high-Mg basalts from Capo Marargiu (Sardinia, Italy): Evidence of cryptic
957 amphibole fractionation in polybaric environments. *J. Volcanol. Geotherm. Res*. **349**, 31–46.
958 Toplis M. J. (2005) The thermodynamics of iron and magnesium partitioning between olivine and
959 liquid: criteria for assessing and predicting equilibrium in natural and experimental systems. *Contrib.*
960 *Mineral. Petrol*. **149**, 22–39.
961 Vetere F., Iezzi G., Behrens H., Cavallo A., Misiti V., Dietrich M., Knipping J., Ventura G. and Mollo
962 S. (2013) Intrinsic solidification behaviour of basaltic to rhyolitic melts: A cooling rate experimental
963 study. *Chem. Geol*. **354**, 233–242.
964 Vetere F., Iezzi G., Behrens H., Holtz F., Ventura G., Misiti V., Cavallo A., Mollo S. and Dietrich
965 M. (2015) Glass forming ability and crystallisation behaviour of sub-alkaline silicate melts. *Earth-*
966 *Sci Rev*. **150**, 25–44.
967 Watson E. B. (1996) Surface enrichment and trace-element uptake during crystal growth. *Geochim.*
968 *Cosmochim. Acta* **60**, 5013–5020.
969 Watson E. B. and Müller T. (2009) Non-equilibrium isotopic and elemental fractionation during
970 diffusion-controlled crystal growth under static and dynamic conditions. *Chem. Geol*. **267**, 111–124.
971 Watson, E. B., Wark, D. A., Price, J. D. and Van Orman J. A. (2002) Mapping the thermal structure
972 of solid-media pressure assemblies. *Contrib. Mineral. Petrol*. **142**, 640–652
973 Weaver S. L., Wallace P. J. and Johnston A. D. (2013) Experimental constraints on the origins of
974 primitive potassic lavas from the Trans-Mexican Volcanic Belt. *Contrib. Mineral. Petrol*. **166**, 825–
975 843.

White J. C. (2003) Trace-element partitioning between alkali feldspar and peralkalic quartz trachyte to rhyolite magma. Part II: Empirical equations for calculating trace-element partition coefficients of large-ion lithophile, high field-strength, and rare-earth elements. *Am. Mineral*. **88**, 330–337.

Wood B. J. and Blundy J. D. (1997) A predictive model for rare earth element partitioning between clinopyroxene and anhydrous silicate melt. *Contrib. Mineral. Petrol*. **129**, 166–181.

Wood B. J. and Blundy J. D. (2001) The effect of cation on crystal-melt partitioning of trace elements. *Earth Planet. Sci. Lett*. **188**, 59–71.

Wood B. J. and Trigila R. (2001) Experimental determination of aluminous clinopyroxene-melt partition coefficients for potassic liquids, with application to the evolution of the Roman province potassic magmas. *Chem. Geol*. **172**, 213–223.

Yagi K. and Onuma K. (1967) The Join $CaMgSi_2O_6$-$CaTiAl_2O_6$ and its bearing on the Titanaugites. J. Fac. Sci. Hokkaido Univ. Ser. *Geol. Mineral*. **13**, 463–483.

Yao L., Sun C. and Liang Y. (2012) A parameterized model for REE distribution between low-Ca pyroxene and basaltic melts with applications to REE partitioning in low-Ca pyroxene along a mantle adiabat and during pyroxenite-derived melt and peridotite interaction. *Contrib. Mineral. Petrol*. **164**, 261–280.

Zhang Y., Ni H. and Chen Y. (2010) Diffusion data in silicate melts. *Rev. Mineral. Geochem*. **72**, 311–408.

Figures captions

Figure 1 Backscattered (BSE) images of experimental samples. Details of the experimental conditions are reported at the bottom of each image. Figures a) and b) show the variation of habit and sizes with time in the runs performed using the glassy starting material (i.e., APR16GL): a) subhedral Cpx with sizes of ~5-10 µm in the shortest run APR16-C2Aa (0.25 hours) and b) euhedral Cpx with sizes up to ~20 µm in the longest run APR16-C2Ad (9 hours); c) Cpx with euhedral habit and size up

to ~50 μm crystallized in the APR16-35 run performed using the natural starting material (i.e., APR16 natural powder). Abbreviation: Cpx: clinopyroxene; Ol: olivine; Gl: glass.

Figure 2 a) Clinopyroxene compositions plotted into the pyroxene classification diagram (Morimoto et al., 1998). Wo: wollastonite; En: enstatite; Fe: ferrosilite. The inset show a magnification of the area of interest. Synthetic samples are indicated with different colours: in orange the runs at 1250 °C, in yellow the runs at 1225 °C, in light blue the runs at 1220 °C, in blue the runs at 1170 °C, in light green the run at 1080 °C. Duration of the experimental runs is indicated with different symbols: circle for 0.25 hours, triangle for 3 hours, diamond for 6 hours and square for 9 hours. b) Composition of the experimental glasses plotted in the TAS diagram (Le Maitre et al., 2002). Coloured bar indicates the variation of temperature of the runs that decreases from red to green. Symbols are as in Figure 2a. Crosses indicate the APR16 (in black) and the APR16GL (in red) starting materials.

Figure 3 C1-normalized (Anders and Grevesse, 1989) trace elements abundances for synthetic clinopyroxenes. Symbols are as in Figure 2. For comparison we reported C1-normalized trace elements abundances for natural Cpx (SCE and SOG samples; Supplementary Material 1), indicated with the grey field.

Figure 4 C1-normalized (Anders and Grevesse, 1989) trace elements abundances for analysed synthetic glasses. Symbols are as in Figure 2. Black crosses indicate data for the APR16 natural samples from Mazzeo et al. (2014). The inset shows a magnification of REE + Y abundances. Yellow field represents REE abundances for natural glasses of Campi Flegrei Volcanic District (CFVD) products (data from GEOROC database; http://georoc.mpch-mainz.gwdg.de/georoc/Start.asp).

Figure 5 Calculated $^{Cpx/L}D$ values for trace elements in experimental samples. Symbols are as in Figure 2. Yellow field represents $^{Cpx/L}D_{REE}$ values for natural Campi Flegrei Volcanic District (CFVD) products (data from Pappalardo et al. (2008), Fedele et al. (2009) and Mollo et al. (2016)).

Figure 6 Onuma diagrams for clinopyroxene-liquid partition coefficients for mono-, di-, tri-, and tetravalent cations versus ionic radii (in Å; Shannon, 1976) for VI- and VIII-fold coordinated sites along with the results of the lattice strain fits in M1 and M2 sites for samples (a) APR16-1C (1225

°C, 3 hours), (b) APR16-35 (1225 °C, 6 hours), (c) APR16-C3Ac (1080 °C, 6 hours) and (d) APR16-C2Bd (1170 °C, 9 hours). The dotted curves represent the fits of the lattice strain model to $^{Cpx/L}D_i$ values while symbols represent measured $^{Cpx/L}D_i$ values. Cations are indicated as follow: monovalent with orange triangles, divalent with yellow squares, trivalent with blue circles and tetravalent with green diamonds. Ba and V (yellow empty square) have not been used in the fit of the LSM for divalent cations. Yellow full squares indicate D_i calculated for M1 and M2 sites. Blue full circle represents D_{Eu} measured in this study, plotted together with the calculated D_{Eu3+} and D_{Eu2+} values (see text for details).

Figure 7 Onuma diagrams showing the variation of predicted REE partitioning between cpx and basaltic melt as function of a) composition (Al^{IV}), and b) composition (Al^{IV}), temperature and undercooling. a) The increase in Al^{IV} content shifts the parabola upward (D_0 increases) and towards left (r_0 decreases); b) the increase in undercooling moves the parabola upward like the Al^{IV} content, while the increase in temperature shifts the parabola downward.

Figure 8 Plot of clinopyroxene-liquid partition coefficients for REEs vs ionic radius (Å). The curves represent the fits of the lattice strain model to $^{Cpx/L}D_i$ values while symbols represent measured $^{Cpx/L}D_i$ values for Dy (HREE), Eu^{3+} (MREE) and Nd (LREE) in the APR16-C2Ad (1220 °C; in light blue), APR16-C1Ac (1250 °C; in orange) and APR16-1C (1225 °C; in yellow) runs. Horizontal arrow indicates the diffusivity decease from LREEs to HREEs, while vertical arrow indicates NBO/T increase and viscosity decrease with decreasing time (from APR16-C2Ad to APR16-1C). On the right side of the figure are reported plots of partition coefficients for Dy, Eu^{3+} and Nd vs NBO/T, in which it is possible to see the negative correlation between *D* values and NBO/T.

Figure 9 Primitive Mantle normalized (McDonough and Sun, 1995) trace elements patterns for primitive basaltic (APR22; D'Antonio et al., 1999) and trachybasaltic (APR19; D'Antonio et al., 1999) rocks, and the predicted composition of differentiated melts obtained after 20 and 28 % of fractional crystallization of APR22 basalt assumed as primitive parental K-basaltic magma. The reported degrees of fractionation (FC) reflect the crystallized phase assemblage and proportions

1053 determined for runs APR16-C2Ad ($Cpx_{(17)}$+$Ol_{(3)}$) and AR16-C2Ab ($Cpx_{(23)}$+$Ol_{(4)}$+$Plg_{(1)}$) that
1054 produced trachybasaltic residual glass. The modelled compositions were calculated by using the
1055 Excel© spreadsheet program of Ersoy and Helvaci (2010) (see §4.3 for details). Normalized patterns
1056 for Campi Flegrei Volcanic District basalts and trachybasalts (D'Antonio et al., 1999; Pappalardo et
1057 al., 1999; De Astis et al., 2004), indicated with red and green field, respectively, are shown for
1058 comparison.
1059
1060 **Tables captions**
1061 **Table 1** Composition (wt.%) of APR16 rock sample, APR16GL starting material, SCE and SOG rock
1062 samples
1063 **Table 2** Experimental conditions of the experimental samples
1064 **Table 3** Major and trace element concentrations (ppm) for synthetic clinopyroxene crystals and
1065 glasses
1066 **Table 4** Major and trace elements partition coefficients between clinopyroxene and glass for
1067 experimental samples
1068 **Table 5** Best fits for E, r_0 and D_0 obtained by regression of clinopyroxene/liquid partition coefficients
1069 of divalent, trivalent and tetravalent cations in M1 and M2 sites
1070
1071 **Supplementary materials**
1072 **Supplementary Material 1** contains information about natural SCE and SOG samples
1073 **Supplementary Material 2** contains supplementary tables
1074 **Supplementary Material 3** contains supplementary figures

Table 1 Composition (wt.%) of APR16 rock sample, APR16GL starting material, SCE and SOG rock samples

Sample	APR16	APR16GL	SCE	SOG
SiO_2	48.89	49.30 (0.46)	47.62	47.78
TiO_2	1.23	1.33 (0.03)	1.23	1.23
Al_2O_3	15.65	15.31 (0.14)	15.33	15.43
FeO_{tot}	8.08	7.79 (0.13)	8.19	8.24
MnO	0.14	0.14 (0.05)	0.14	0.15
MgO	8.89	9.31 (0.07)	9.78	9.75
CaO	11.64	12.02 (0.09)	11.89	11.59
Na_2O	2.88	2.86 (0.05)	2.69	2.83
K_2O	1.52	1.60 (0.02)	1.58	1.67
P_2O_5	0.31	0.55 (0.02)	0.29	0.29
Total	99.99	99.31 (0.29)[§]	99.65	99.88
L.O.I.	0.61	-	0.26	0.28
Mg# [1]	0.66	0.68	0.68	0.68

Notes: [1][MgO/(MgO + FeO_{tot})] molar, assuming all Fe^{2+} and Fe^{3+} as FeO_{tot}. Chemical composition of APR16 is from D'Antonio et al. (1999); APR16GL composition is from Perinelli et al. (2019); SCE and SOG from Bonechi et al. (2020b). § For APR16GL the analysis is normalized to 100 % but the original total is reported. Standard deviation is reported in parenthesis.

.

Table 2

Table 2 Experimental conditions of the experimental samples

Runs	Starting material	P (GPa)	T (°C)	ΔT (°C)	Time (h)	G_{LCpx} (cm s^{-1})	H_2O_i (wt.%)	H_2O_f (wt.%)	NBO/ T	Phases	Σr^2	% ΔFe§	References
APR16-1C	APR16	0.8	1225	55	3	$1.59 \cdot 10^{-7}$	NWA	0.96±0.29	0.82	Gl(94) + Cpx(6) + Ol# + Ox#	0.38	-5	Bonechi (2020)
APR16-35	APR16	0.8	1225	55	6	$8.34 \cdot 10^{-8}$	NWA	1.7±0.42	0.80	Gl(96) + Cpx(4) + Ol#	0.14	-22	
APR16-C1Ac	APR16GL	0.8	1250	45	6	$2.06 \cdot 10^{-8}$	NWA	2.03±0.43	0.78	Gl(83) + Cpx(15) + Ol(2)	0.83	-20	Bonechi et al. (2020b)
APR16-C1Ad	APR16GL	0.8	1250	45	9	$1.73 \cdot 10^{-8}$	NWA	1.95±0.38	0.85	Gl(90) + Cpx(10)	0.65	-19	
APR16-C2Aa	APR16GL	0.8	1220	50	0.25	$3.24 \cdot 10^{-7}$	2	1.92±0.34	0.92	Gl(91) + Cpx(4) + Ol(1) + Ox(4)	0.02	-25	
APR16-C2Ab	APR16GL	0.8	1220	50	3	$3.04 \cdot 10^{-8}$	1.9	1.56±0.36	0.61	Gl(72) + Cpx(23) + Ol(4) + Plg(1) + Ox*	0.66	-17	
APR16-C2Ac	APR16GL	0.8	1220	50	6	$2.67 \cdot 10^{-8}$	2.1	2.47±0.35	0.60	Gl(65) + Cpx(27) + Ol(5) + Plg(3)	0.93	-25	
APR16-C2Ad	APR16GL	0.8	1220	50	9	$1.93 \cdot 10^{-8}$	1.9	1.3±0.38	0.70	Gl(80) + Cpx(17) + Ol(3) + Ox*	0.25	-26	
APR16-C2Bc	APR16GL	0.8	1170	100	6	$2.77 \cdot 10^{-8}$	2	3.77±0.1	0.67	Gl(58) + Cpx(33) + Ol(5) + Plg(1)	0.73	-27	
APR16-C2Bd	APR16GL	0.8	1170	100	9	$2.34 \cdot 10^{-8}$	1.8	2.02±0.46	0.61	Gl(57) + Cpx(34) + Ol(2) + Plg(3) + Ox(4)	0.56	-4	
APR16-C3Ac	APR16GL	0.8	1080	144	6	$1.31 \cdot 10^{-8}$	3.8	6.5±0.35	1.00	Gl(60) + Cpx(37) + Ol(3)	0.62	-10	Bonechi et al. (2020a)

Notes: Gl = glass; Cpx = clinopyroxene; Ol = Olivine; Plg = plagioclase; Ox = oxide; NWA = No Water Added. ΔT is the difference between the Cpx liquidus temperature and the nominal temperature of the runs; G_{LCpx} is the Cpx growth rate taken from Bonechi et al. (2020b); H_2O_i is nominal content (wt.%) of water added to the charge; H_2O_f = water content in the melt determined by the by-difference calculation method (respect to the total of EMP analyses); NBO/T is the ratio of non-bridging oxygens to number of structural tetrahedra in the liquid calculated as in Mysen (1985) considering the H_2O_f of the runs. Σr^2 values from mass balance calculation. § Percent of relative Fe loss from starting material based on difference between the starting material and calculated bulk composition of experiment obtained from mass-balance calculations.* crystals present in trace; # pre-existing crystals.

Table 3

Table 3 Major and trace element concentrations (ppm) for synthetic clinopyroxene crystals and glasses

Run#	APR16-1C	APR16-35	APR16-C1Ac	APR16-C1Ad	APR16-C2Aa	APR16-C2Ab	APR16-C2Ac	APR16-C2Ad	APR16-C2Bc	APR16-C2Bd	APR16-C3Ac
Phase	cpx glass	cpx glass	cpx glass	cpx glass	cpx glass	cpx glass	cpx glass	cpx glass	cpx glass	cpx glass	cpx glass
Na	2560 (838) 23215 (275)	2950 (307) 22163 (225)	3709 (351) 25074 (213)	3709 (265) 23591 (203)	3041 (*302*) 21365 (211)	4525 (*452*) 23665 (198)	6083 (*433*) 23294 (231)	3561 (*363*) 22107 (220)	bdl -	5638 (*502*) 28339 (223)	4154 (341) 27226 (207)
K	279 (102) 14562 (291)	103 (52) 14693 (204)	581 (103) 15772 (206)	498 (98) 14942 (232)	581 (*92*) 13033 (243)	1909 (*232*) 17599 (221)	1826 (*312*) 20754 (209)	415 (*105*) 16270 (214)	bdl -	1079 (*343*) 21916 (225)	913 (123) 15275 (213)
Ca	150086 (5800) 73870 (1250)	150086 (6100) 74268 (1130)	129450 (5980) 71242 (3850)	147514 (4800) 80403 (2100)	137400 (*6400*) 86335 (4120)	145155 (*5100*) 76620 (3560)	146086 (*4350*) 58748 (3400)	152874 (*5210*) 77187 (2980)	bdl -	146585 (*4600*) 56533 (3230)	153017 (3980) 67039 (4550)
Fe	38643 (4451) 61647 (1208)	22399 (2350) 30246 (903)	32569 (2310) 48193 (950)	34357 (1890) 48193 (860)	35134 (*1930*) 44696 (810)	34823 (*2100*) 42519 (950)	34357 (*1850*) 42674 (890)	31248 (*2210*) 34901 (730)	bdl -	42130 (*1900*) 47183 (1010)	45317 (2530) 46950 (980)
Mg	84353 (6092) 43253 (507)	96961 (6310) 45112 (466)	90573 (11665) 46575 (1800)	95300 (7600) 46456 (1540)	81600 (*4300*) 44060 (1480)	108000 (*16000*) 45660 (1840)	87000 (*8200*) 47100 (3125)	110000 (*13000*) 32183 (1225)	5900 (110) 28075 (2869)	83000 (*7900*) 33100 (1925)	86933 (4600) 33280 (1580)
Al	25520 (6890) 83792 (2340)	28709 (7650) 83050 (3050)	59765 (15843) 94219 (3525)	41540 (5760) 92220 (3100)	22900 (*2200*) 73560 (3080)	28700 (*160*) 128750 (11675)	41070 (*3000*) 105150 (4800)	36500 (*1700*) 96220 (6920)	5750 (95) 102650 (3830)	36300 (*3300*) 103575 (5925)	37783 (1700) 99238 (3920)
Mn	880 (130) 1151 (10)	915 (82) 1127 (13)	900 (110) 1211 (12)	1100 (199) 1296 (30)	1080 (*320*) 1136 (21)	1140 (*170*) 1299 (35)	1143 (*95*) 1310 (172)	1210 (120) 1359 (43)	bdl 1185 (107)	1054 (*92*) 1307 (42)	1271 (97) 1254 (28)
Ti	4370 (259) 7296 (92)	4257 (1041) 7395 (113)	2684 (29) 7070 (40)	3275 (1136) 7180 (90)	3570 (*910*) 6432 (100)	3510 (*570*) 8253 (388)	4440 (*650*) 6405 (61)	6410 (*670*) 7906 (205)	bdl 7575 (367)	8050 (*870*) 8625 (128)	5270 (139) 7526 (150)
Zr	34 (11) 103 (2)	31 (2) 105 (2)	18 (3) 111 (5)	33 (10) 111 (2)	bdl 99 (2)	26 (*9*) 129 (*7*)	33 (*7*) 198 (9)	60 (*12*) 120 (1)	bdl 133 (5)	82 (*12*) 143 (2)	40 (2) 128 (2)
Nb	0.11 (0.07) 13.1 (0.3)	0.20 (0.04) 13.1 (0.3)	bdl 13.7 (0.5)	1.1 (0.6) 12.7 (0.6)	bdl 10.2 (0.6)	2.4 (0.3) 15 (1)	bdl 26.2 (0.1)	bdl 14 (1)	bdl 17 (2)	bdl 18 (1)	0.7 (0.1) 14.1 (0.4)
Hf	1.6 (0.4) 2.5 (0.2)	1.6 (0.2) 2.6 (0.1)	bdl 2.8 (0.1)	bdl 2.85 (0.03)	bdl 2.2 (0.1)	bdl 2.8 (0.3)	1.2 (0.2) 3.8 (0.2)	2 (1) 2.7 (0.3)	bdl 2.9 (0.3)	3.9 (1.4) 3.3 (0.4)	1.8 (0.2) 3.3 (0.4)
Ta	0.05 (0.01) 0.68 (0.04)	0.04 (0.01) 0. 67 (0.04)	bdl 0.7 (0.2)	bdl 0.7 (0.1)	bdl 0.5 (0.1)	bdl 0.85 (0.05)	bdl 1.5 (0.2)	bdl 0.8 (0.1)	bdl 0.99 (0.13)	bdl 1.04 (0.16)	bdl 0.9 (0.1)
Th	0.06 (0.01) 2.9 (0.1)	0.06 (0.02) 2.9 (0.1)	bdl 3.4 (0.2)	bdl 3.3 (0.2)	bdl 2.5 (0.1)	bdl 3.6 (0.4)	bdl 6.3 (0.8)	bdl 3.2 (0.3)	bdl 4.1 (0.4)	bdl 4.9 (0.3)	0.20 (0.06) 3.7 (0.3)
U	0.01 0.93 (0.05)	0.03 (0.01) 0.94 (0.04)	bdl 1.0 (0.1)	bdl 1.2 (0.1)	bdl 0.8 (0.1)	bdl 1.1 (0.1)	bdl 2.24 (0.04)	bdl 1.1 (0.2)	bdl 1.4 (0.1)	bdl 1.5 (0.2)	bdl 1.2 (0.2)
Rb	bdl 57 (1)	bdl 56 (1)	bdl 64 (2)	11 (*3*) 66 (1)	bdl 53.1 (0.1)	bdl 71 (2)	8 (*4*) 120 (4)	bdl 69 (4)	bdl 78 (6)	bdl 95 (1)	2.2 (0.3) 70 (3)
Sr	54 (8) 503 (6)	52 (2) 499 (5)	59 (1) 531 (2)	83 (*8*) 540 (6)	55 (*16*) 442 (4)	71 (*18*) 631 (13)	87 (*16*) 698 (15)	84 (*13*) 594 (8)	bdl 652 (21)	60 (*8*) 693 (26)	78 (6) 605 (3)
Cs	bdl 2.4 (0.1)	bdl 2.4 (0.1)	bdl 2.7 (0.2)	bdl 3.0 (0.2)	bdl 2.2 (0.3)	bdl 3.3 (0.3)	bdl 4.8 (0.1)	bdl 2.9 (0.1)	bdl 3.3 (0.5)	bdl 3.9 (0.2)	bdl 3.0 (0.3)
Ba	0.41 (0.01) 534 (9)	0.76 (0.37) 532 (7)	12 (7) 536 (7)	30 (13) 553 (17)	16 (9) 450 (2)	bdl 670 (39)	43 (22) 1013 (43)	15 (7) 589 (4)	bdl 773 (4)	bdl 749 (29)	20.8 (0.6) 606 (1)

Pb	0.12 (0.15)	0.14 (0.05)	bdl	bdl	bdl	bdl	bdl	bdl	bdl	bdl	bdl
	1.1 (0.5)	11.7 (0.4)	bdl	bdl	0.9 (0.1)	bdl	bdl	bdl	bdl	bdl	bdl
Sc	119 (21)	113 (5)	80 (10)	87 (8)	87 (*27*)	110 (*13*)	88 (5)	112 (19)	bdl	155 (14)	93 (3)
	28 (1)	30 (1)	40 (1)	40 (2)	40 (1)	27 (3)	23 (1)	43 (2)	19 (1)	22 (1)	26 (1)
V	248 (23)	764 (86)	120 (16)	174 (49)	133 (*17*)	237 (*43*)	263 (*41*)	385 (*36*)	bdl	505 (*50*)	199 (8)
	190 (2)	162 (4)	201 (5)	194 (4)	184 (2)	182 (4)	180 (6)	217 (4)	157 (2)	198 (1)	224 (3)
Cr	3229 (708)	4460 (605)	4445 (345)	2390 (1259)	2210 (*44*)	1740 (*600*)	1100 (*120*)	1200 (*190*)	bdl	1400 (*230*)	1617 (92)
	80 (12)	96 (9)	77 (23)	57 (1)	318 (2)	35 (*17*)	31 (*11*)	163 (3)	bdl	28 (*12*)	26 (*13*)
Co	28 (2)	15 (3)	22 (5)	33 (2)	26 (*11*)	13 (*7*)	19 (*4*)	21 (*9*)	bdl	43 (*5*)	36 (1)
	34 (2)	12 (1)	24 (1)	25 (1)	27 (1)	19 (1)	17 (1)	17 (1)	10 (1)	15 (1)	21 (10)
Ni	139 (12)	44 (18)	37 (*17*)	60 (*6*)	bdl	51 (*18*)	bdl	bdl	bdl	137 (*18*)	177 (10)
	43 (9)	7 (1)	15 (2)	26 (2)	33 (1)	12 (1)	8 (2)	9 (1)	bdl	9 (1)	12 (1)
Y	15 (2)	17 (1)	17 (2)	bdl	bdl	bdl	bdl	bdl	bdl	bdl	bdl
	19.9 (0.3)	20.2 (0.3)	19 (1)	bdl	bdl	bdl	bdl	bdl	bdl	bdl	bdl
La	1.9 (0.4)	1.8 (0.2)	bdl	1.5 (*0.5*)	bdl	2.6 (*1.1*)	bdl	3.9 (*1.7*)	bdl	4.7 (*1.2*)	3 (0.2)
	15.6 (0.3)	16.01 (0.24)	17.1 (0.5)	17.9 (0.3)	14.7 (0.2)	20.9 (0.9)	33 (2)	19 (1)	22 (1)	25 (2)	20 (1)
Ce	7.3 (1.7)	6.7 (0.7)	6.7 (0.3)	5.8 (3.4)	bdl	7.8 (*2.3*)	bdl	11.2 (*3.5*)	bdl	13 (*2*)	10.1 (0.5)
	34.5 (0.5)	35.1 (0.6)	36 (1)	37 (1)	30 (1)	42 (1)	67 (4)	37 (1)	45.2 (0.5)	49 (2)	41 (1)
Pr	1.4 (0.3)	1.3 (0.1)	1.8 (0.3)	1.1 (*0.4*)	bdl	1.6 (*0.7*)	1.4 (*0.2*)	2.1 (*0.3*)	bdl	2.6 (*0.5*)	1.9 (0.1)
	4.4 (0.1)	4.5 (0.1)	4.5 (0.2)	5.2 (0.1)	3.9 (0.3)	5 (0.5)	7.8 (1.2)	4.9 (0.2)	5.1 (0.2)	5.9 (0.3)	5.2 (0.3)
Nd	8.5 (1.5)	7.9 (0.7)	11 (1)	7.2 (2.1)	bdl	8.3 (*4.2*)	7.2 (*0.9*)	14 (*5*)	bdl	16 (*3*)	11.7 (0.4)
	19 (1)	19.4 (0.5)	20 (1)	23 (2)	17 (1)	24 (2)	35 (4)	21 (2)	22 (1)	25 (2)	24 (1)
Sm	3.02 (0.61)	3.03 (0.4)	3.4 (0.6)	3.8 (*0.2*)	bdl	bdl	bdl	bdl	bdl	5.5 (*2.2*)	4.4 (1.1)
	4.5 (0.3)	4.7 (0.3)	4.89 (0.03)	5.9 (0.6)	4.4 (0.6)	5.4 (1)	7.7 (0.8)	5.3 (0.6)	5.4 (0.4)	6.1 (1.5)	5.8 (0.4)
Eu	0.9 (0.1)	0.8 (0.1)	0.9 (0.2)	bdl	bdl	bdl	0.8 (0.1)	bdl	bdl	1.1 (*0.4*)	1.5 (0.2)
	1.5 (0.1)	1.5 (0.1)	1.6 (0.2)	1.9 (0.6)	1.5 (0.2)	1.8 (0.2)	2.5 (0.2)	1.9 (0.3)	1.6 (0.5)	1.9 (0.2)	1.7 (0.1)
Gd	3.7 (0.4)	3.5 (0.3)	3.1 (*0.2*)	2.7 (*0.2*)	bdl	bdl	bdl	5.1 (1.6)	bdl	5.8 (*2.1*)	4.9 (0.9)
	4.5 (0.2)	4.4 (0.3)	4.6 (0.4)	5.5 (0.6)	4.1 (0.4)	4.8 (0.7)	6.3 (0.3)	5.3 (0.3)	4.4 (0.5)	5.8 (1.2)	5.1 (0.8)
Tb	0.53 (0.07)	0.57 (0.05)	bdl	0.44 (*0.1*)	bdl	bdl	0.38 (*0.05*)	bdl	bdl	1.1 (*0.3*)	0.68 (0.05)
	0.63 (0.04)	0.66 (0.05)	0.66 (0.01)	0.74 (0.16)	0.59 (0.08)	0.86 (0.09)	1.02 (0.23)	0.76 (0.13)	0.72 (0.11)	0.88 (0.17)	0.73 (0.11)
Dy	3.3 (0.4)	3.52 (0.05)	3.9 (1.2)	2.6 (*0.8*)	bdl	bdl	bdl	5.8 (*0.4*)	bdl	4.7 (*1.7*)	4.4 (0.5)
	3.8 (0.2)	3.9 (0.2)	3.8 (0.1)	4.5 (0.4)	3.6 (0.3)	4.9 (0.4)	5.6 (0.2)	4.1 (0.4)	4.2 (0.6)	4.2 (0.2)	4.2 (0.3)
Ho	0.64 (0.07)	0.66 (0.05)	0.76 (0.21)	bdl	bdl	0.59 (0.33)	bdl	bdl	bdl	0.89 (*0.39*)	0.84 (0.12)
	0.75 (0.05)	0.77 (0.04)	0.81 (0.1)	0.92 (0.18)	0.65 (0.08)	0.93 (0.16)	1.13 (0.22)	0.81 (0.14)	0.80 (0.14)	0.90 (0.12)	0.90 (0.12)
Er	1.59 (0.27)	1.75 (0.18)	1.53 (0.34)	1.12 (*0.11*)	bdl	bdl	bdl	bdl	bdl	2.62 (*0.95*)	2.14 (0.12)
	2.12 (0.13)	2.04 (0.15)	2.04 (0.19)	2.31 (0.29)	1.94 (0.18)	2.22 (0.19)	3.07 (0.6)	2.14 (0.2)	2.09 (0.35)	2.15 (0.3)	2.11 (0.34)
Tm	0.20 (0.03)	0.22 (0.03)	0.19 (0.08)	bdl	bdl	bdl	bdl	bdl	bdl	bdl	0.32 (0.04)
	0.27 (0.02)	0.29 (0.04)	0.28 (0.02)	0.36 (0.05)	0.25 (0.03)	0.32 (0.03)	0.37 (0.04)	0.31 (0.04)	bdl	0.30 (0.05)	0.28 (0.09)
Yb	1.24 (0.22)	1.43 (0.16)	bdl	bdl	bdl	bdl	bdl	bdl	bdl	bdl	1.73 (0.29)
	1.78 (0.15)	1.87 (0.21)	1.91 (0.38)	2.34 (0.17)	1.87 (0.32)	2.07 (0.44)	2.65 (0.07)	2.01 (0.27)	2.01 (0.57)	2.26 (0.3)	1.78 (0.68)
Lu	0.17 (0.02)	0.21 (0.01)	bdl	bdl	bdl	bdl	bdl	bdl	bdl	bdl	0.26 (0.03)
	0.27 (0.03)	0.27 (0.02)	0.29 (0.06)	0.36 (0.06)	0.28 (0.08)	0.33 (0.03)	0.49 (0.12)	0.33 (0.04)	0.31 (0.03)	0.4 (0.09)	0.31 (0.05)

Notes: cpx = clinopyroxene; standard deviation is reported in brackets.

For single analysis Int2SE (i.e., analytical error) is reported also in brackets but in italic; bdl = below detection limit.

Table 4 Major and trace elements partition coefficients between clinopyroxene and glass for experimental samples

Run#	APR16-1C	APR16-35	APR16-C1Ac	APR16-C1Ad	APR16-C2Aa	APR16-C2Ab	APR16-C2Ac	APR16-C2Ad	APR16-C2Bd	APR16-C3Ac
Na	0.11 (0.01)	0.13 (0.02)	0.15 (0.01)	0.16 (0.02)	0.14 (0.02)	0.19 (0.02)	0.26 (0.03)	0.16 (0.01)	0.20 (0.03)	0.15 (0.01)
K	0.019 (0.001)	0.007 (0.001)	0.04 (0.01)	0.03 (0.01)	0.04 (0.01)	0.11 (0.01)	0.088 (0.005)	0.026 (0.005)	0.05 (0.01)	0.042 (0.002)
Ca	2.03 (0.14)	2.02 (0.03)	1.82 (0.15)	1.83 (0.15)	1.59 (0.12)	1.89 (0.12)	2.47 (0.25)	1.98 (0.15)	2.59 (0.25)	2.28 (0.13)
Fe	0.59 (0.07)	0.61 (0.08)	0.66 (0.08)	0.69 (0.08)	0.77 (0.08)	0.77 (0.08)	0.78 (0.08)	0.88 (0.08)	0.87 (0.08)	0.97 (0.09)
Fe_{M1}	0.293	0.367	0.329	0.421		0.410	0.411	0.45	0.535	0.672
Fe_{M2}	0.297	0.247	0.329	0.268		0.358	0.372	0.43	0.338	0.293
Mg	1.94 (0.04)	1.92 (0.07)	2.23 (0.24)	2.12 (0.72)	1.85 (0.12)	2.41 (0.37)	2.55 (0.38)	2.03 (0.14)	2.5 (0.3)	2.68 (0.27)
Mg_{M1}	1.809	1.811	2.074	1.991		2.232	2.382	1.809	2.353	2.552
Mg_{M2}	0.135	0.106	0.158	0.129		0.18	0.167	0.219	0.143	0.129
Al	0.42 (0.12)	0.38 (0.12)	0.33 (0.17)	0.29 (0.06)	0.36 (0.03)	0.36 (0.04)	0.46 (0.02)	0.35 (0.02)	0.49 (0.04)	0.37 (0.02)
Al_T	0.225	0.185	0.181	0.155	0.187	0.167	0.222	0.199	0.257	0.199
Al_{M1}	0.191	0.192	0.153	0.137	0.169	0.189	0.242	0.148	0.233	0.171
Mn	0.72 (0.36)	0.63 (0.21)	0.75 (0.41)	0.62 (0.27)		0.74 (0.20)	0.91 (0.25)	0.91 (0.37)	0.85 (0.28)	0.74 (0.30)
Ti	0.56 (0.15)	0.58 (0.09)	0.38 (0.09)	0.46 (0.12)	0.55 (0.14)	0.42 (0.07)	0.69 (0.07)	0.81 (0.11)	0.93 (0.12)	0.70 (0.06)
Zr	0.33 (0.11)	0.30 (0.02)	0.16 (0.03)	0.3 (0.1)		0.20 (0.01)	0.16 (0.01)	0.500 (0.004)	0.57 (0.01)	0.31 (0.02)
Nb	0.008 (0.005)	0.015 (0.003)		0.087 (0.004)			0.094 (0.001)			0.05 (0.01)
Hf	0.67 (0.17)	0.62 (0.08)					0.31 (0.01)	0.73 (0.08)	1.19 (0.13)	0.56 (0.09)
Ta	0.07 (0.01)	0.06 (0.01)								
Th	0.020 (0.005)	0.02 (0.01)								0.055 (0.001)
U	0.011 (0.001)	0.03 (0.01)								
Rb				0.166 (0.003)			0.068 (0.003)			0.031 (0.003)
Sr	0.11 (0.02)	0.104 (0.004)	0.111 (0.002)	0.153 (0.002)	0.122 (0.001)	0.106 (0.002)	0.125 (0.003)	0.141 (0.002)	0.086 (0.003)	0.13 (0.01)
Ba	0.001 (0.001)	0.001 (0.001)	0.0232 (0.0003)	0.054 (0.002)	0.0349 (0.0002)		0.042 (0.002)	0.0248 (0.0002)		0.034 (0.001)
Pb	0.11 (0.05)	0.012 (0.004)								
Sc	4.24 (0.74)	3.74 (0.19)	2.01 (0.26)	2.18 (0.23)	2.20 (0.08)	4.09 (0.40)	3.84 (0.17)	2.58 (0.12)	7.06 (0.24)	3.60 (0.18)

V	1.30 (0.12)	4.71 (0.54)	0.597 (0.083)	0.892 (0.252)	0.722 (0.008)	1.31 (0.03)	1.46 (0.04)	1.77 (0.03)	2.55 (0.01)	0.886 (0.037)
Cr	41 (11)	47 (8)	57 (18)	42 (22)	6.9 (0.1)	50	35	7.3 (1.2)	50	63 (4)
Co	0.83 (0.07)	1.25 (0.23)	0.92 (0.21)	1.32 (0.08)	0.95 (0.40)	0.68 (0.38)	1.12 (0.24)	1.21 (0.52)	2.87 (0.35)	1.71 (0.78)
Co_{M1}	0.64	1.11	0.71	1.15		0.46	0.9	0.93	2.67	1.54
Co_{M2}	0.18	0.14	0.2	0.17		0.22	0.22	0.28	0.19	0.17
Ni	3.21 (0.71)	6.29 (2.81)	2.38 (1.17)	2.33 (0.28)		4.31 (0.43)			15.6 (2.3)	15 (2)
Y	0.77 (0.10)	0.85 (0.03)	0.89 (0.12)							
La	0.12 (0.03)	0.11 (0.01)		0.082 (0.001)		0.124 (0.005)		0.20 (0.01)	0.19 (0.01)	0.15 (0.09)
Ce	0.21 (0.05)	0.19 (0.02)	0.19 (0.01)	0.16 (0.09)	0.19 (0.01)			0.28 (0.01)	0.25 (0.01)	0.25 (0.01)
Pr	0.33 (0.07)	0.29 (0.03)	0.4 (0.1)	0.213 (0.005)		0.31 (0.03)	0.18 (0.03)	0.42 (0.01)	0.44 (0.02)	0.36 (0.03)
Nd	0.45 (0.08)	0.41 (0.03)	0.53 (0.07)	0.31 (0.09)		0.35 (0.02)	0.21 (0.02)	0.64 (0.05)	0.66 (0.04)	0.49 (0.03)
Sm	0.67 (0.14)	0.65 (0.09)	0.69 (0.13)	0.64 (0.06)					0.90 (0.03)	0.77 (0.17)
Eu	0.64 (0.1)	0.54 (0.06)	0.59 (0.13)				0.31 (0.02)		0.57 (0.06)	0.84 (0.13)
Eu^{2+}	0.137	0.132	0.140	0.193				0.179	0.111	0.169
Eu^{3+}	0.756	0.729	0.772	0.718				1.071	1.032	0.877
Gd	0.82 (0.13)	0.78 (0.09)	0.67 (0.06)	0.49 (0.05)				0.95 (0.05)	1.01 (0.20)	0.97 (0.23)
Tb	0.83 (0.12)	0.87 (0.11)		0.59 (0.13)			0.38 (0.08)		1.29 (0.25)	0.93 (0.15)
Dy	0.86 (0.11)	0.90 (0.05)	1.02 (0.32)	0.59 (0.05)				1.40 (0.13)	1.12 (0.05)	1.04 (0.14)
Ho	0.85 (0.10)	0.86 (0.08)	0.94 (0.28)			0.64 (0.11)			0.99 (0.13)	0.93 (0.18)
Er	0.75 (0.13)	0.86 (0.08)	0.75 (0.18)	0.49 (0.06)					1.22 (0.17)	1.01 (0.17)
Tm	0.75 (0.12)	0.77 (0.15)	0.68 (0.29)							1.14 (0.39)
Yb	0.70 (0.13)	0.76 (0.12)								0.97 (0.40)
Lu	0.62 (0.11)	0.75 (0.07)								0.83 (0.16)

Notes: standard deviation is reported in brackets. D_{M1} and D_{M2}, and Eu^{2+} and Eu^{3+} partition coefficients were recalculated following the procedure described in section 4.1.

Table 5

Table 5 Best fits for E, r_0 and D_0 obtained by regression of clinopyroxene/liquid partition coefficients of divalent, trivalent and tetravalent cations in M1 and M2 sites

Run#	APR16-1C	APR16-35	APR16-C1Ac	APR16-C1Ad	APR16-C2Aa	APR16-C2Ab	APR16-C2Ac	APR16-C2Ad	APR16-C2Bd	APR16-C3Ac
M2^{2+}										
D_0	2.38±0.29	2.38±0.49	2.25±0.33	2.02±0.71	2.31±0.07	2.27±0.40	3.07±0.47	2.46±0.38	3.19±0.49	2.68±0.32
r_0	1.081±0.005	1.083±0.002	1.079±0.005	1.088±0.003	1.059±0.001	1.077±0.006	1.081±0.006	1.078±0.005	1.080±0.003	1.084±0.004
r_0 (WB97)	*1.081*	*1.082*	*1.082*	*1.083*		*1.079*	*1.076*	*1.084*	*1.078*	*1.084*
E	271±22	287±20	260±24	246±31	200±20	252±29	274±27	236±22	286±19	249±18
E (WB97)	*180*	*180*	*179*	*179*		*180*	*180*	*180*	*181*	*183*
M1^{2+}										
D_0	5.34±1.35	7.07±3.11	4.64±1.84	3.74±1.01		6.55±1.27	6.50±2.65	3.47±0.78	9.95±0.07	7.37±1.92
r_0	0.616±0.014	0.610±0.011	0.621±0.013	0.639±0.013		0.614±0.013	0.617±0.012	0.646±0.009	0.634±0.004	0.634±0.009
E	504±133	461±60	484±72	523±148		473±82	468±54	530±74	596±5	455±77
M2^{3+}										
D_0	0.860±0.006	0.857±0.002	0.879±0.001	0.614±0.001		0.653±0.005	0.373±0.008	1.165±0.013	1.128±0.002	1.139±0.008
r_0	1.0297±0.0002	1.0257±0.0005	1.0300±0.0002	1.022±0.001		1.033±0.001	1.033±0.001	1.0301±0.0003	1.0323±0.0003	1.0292±0.0005
r_0 (WB97)	*1.0208*	*1.0221*	*1.0220*	*1.023*		*1.019*	*1.016*	*1.0239*	*1.0177*	*1.0245*
E	325±6	326±3	322±1	307±4		305±3	304±3	304±1	310±4	300±2
E (WB97)	*270*	*270*	*269*	*269*		*270*	*270*	*270*	*272*	*275*
M1^{3+}										
D_0	40.05±0.07	40.07±0.10	40.12±0.28	40.05±0.11	11.01±0.55	40.07±0.11	40.03±0.06	20.04±0.05	42.21±1.99	40.11±0.51
r_0	0.664±0.008	0.665±0.006	0.654±0.004	0.655±0.017	0.664±0.002	0.661±0.002	0.660±0.01	0.666±0.001	0.672±0.001	0.663±0.001
E	1499±2	1499±1	1499±1	1499±5	1202±48	1499±1	1499±1	1499±1	1499±4	1499±1
M1^{4+}										
D_0	3.60±1.29	3.50±1.31					1.98±0.83	2.52±0.99	6.21±1.82	2.31±0.94
r_0	0.659±0.001	0.659±0.001					0.650±0.005	0.658±0.002	0.660±0.001	0.656±0.002
r_0 (H11)	*0.649±0.007*	*0.649±0.007*	*0.649±0.007*	*0.649±0.007*	*0.649±0.007*	*0.649±0.007*	*0.649±0.007*	*0.649±0.007*	*0.649±0.007*	*0.649±0.007*
E	3077±559	3115±634					2404±703	1967±623	3014±518	2024±578
E (H11)	*2936±722*	*2936±722*	*2936±722*	*2936±722*	*2936±722*	*2936±722*	*2936±722*	*2936±722*	*2936±722*	*2936±722*

Note: D_0: strain-compensated partition coefficient. E: Young Modulus of the lattice site (GPa). r_0: optimum site radius (Å). D_0, r_0 and E were calculated using the SIMPLE and DOUBLE FIT program (Dalou et al., 2018). Values in italic are the lattice strain parameters $r_0^{2+,+3}$ and $E^{2+,+3}$ for the M2 site calculated by the relations of Wood and Blundy (1997), and the average r_0^{4+} and E^{4+} values obtained for the M1 site of clinopyroxene by Hill et al. (2011).

Figure 1

Click here to access/download;Figure;Figure 1.png

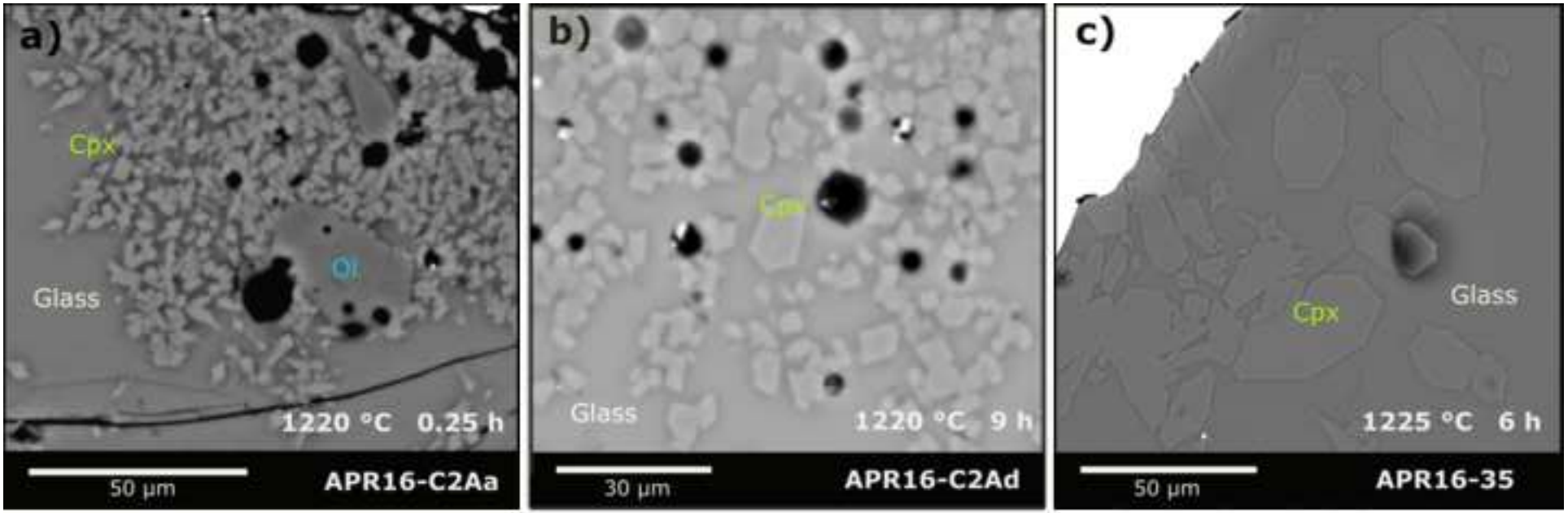

Figure 2

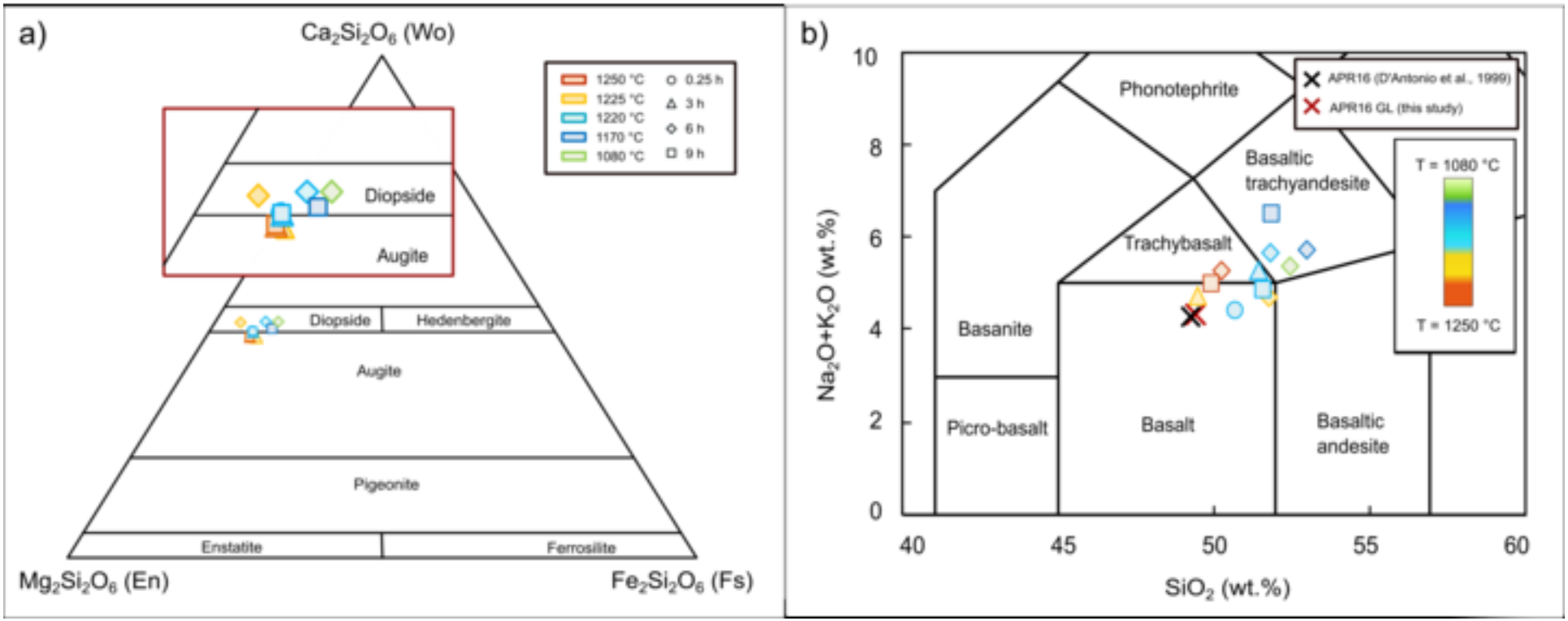

Figure 3

Click here to access/download;Figure;Figure 3.png

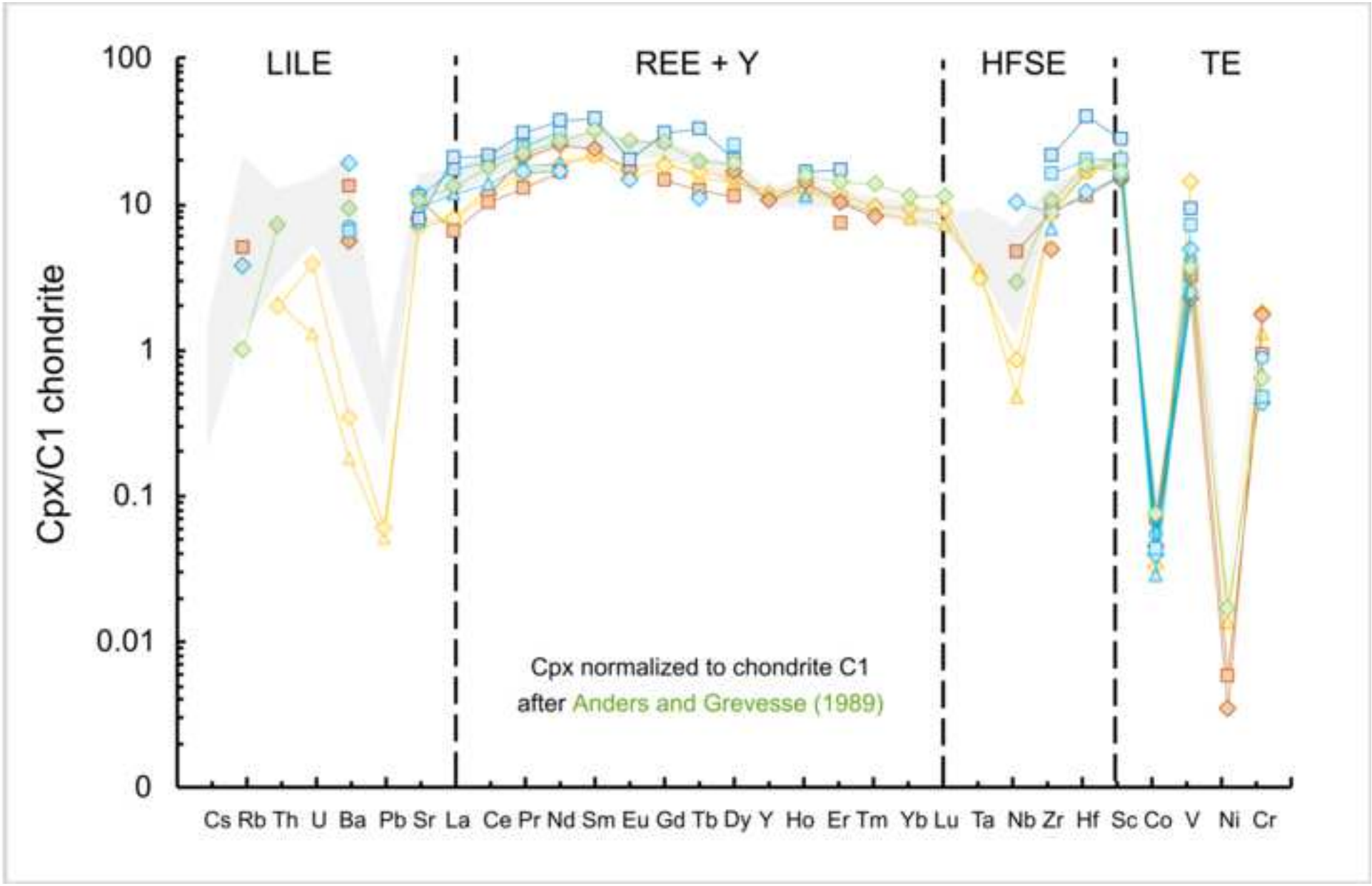

Figure 4

Click here to access/download;Figure;Figure 4.png

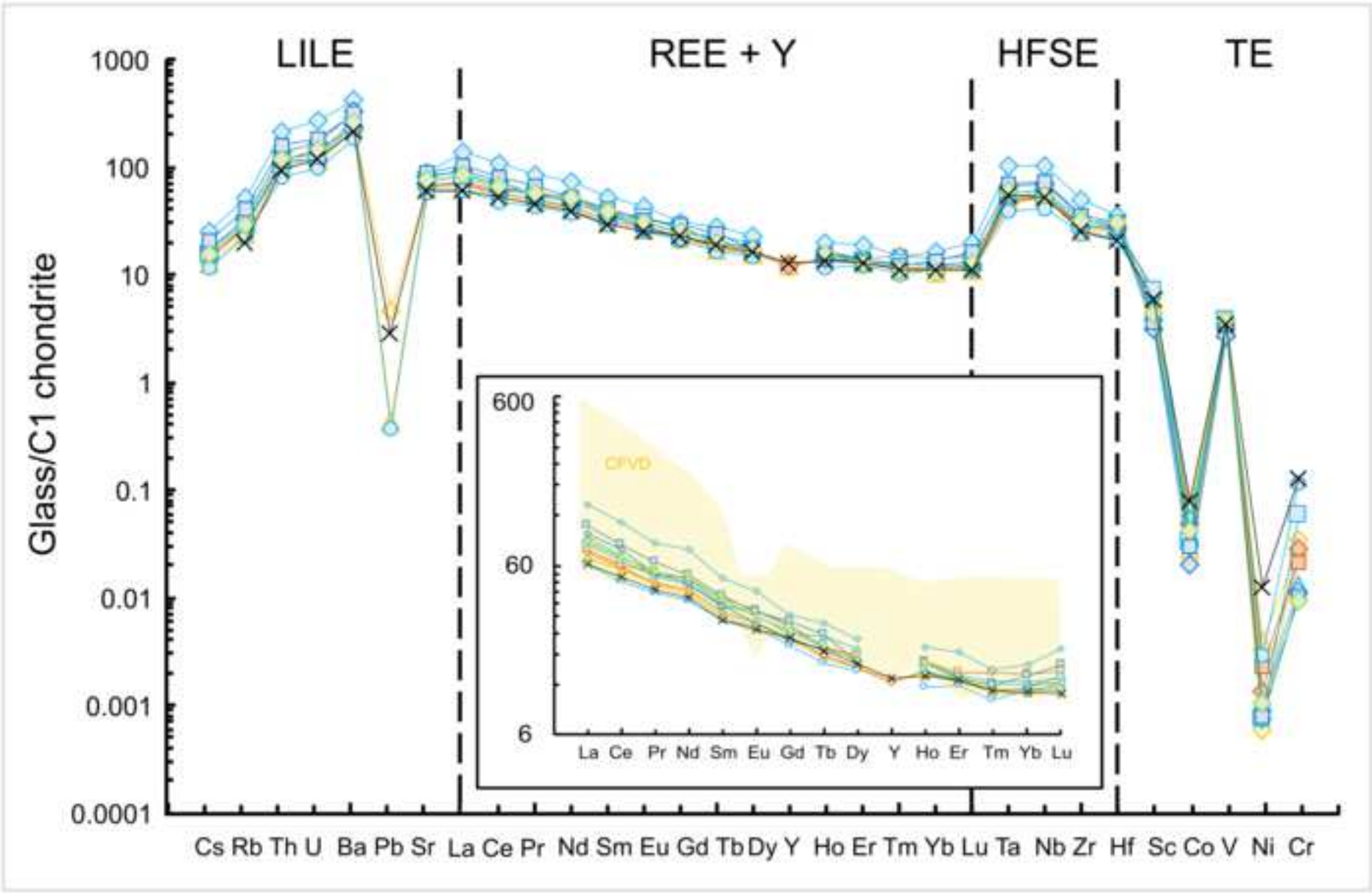

Figure 5

Click here to access/download;Figure;Figure 5.png

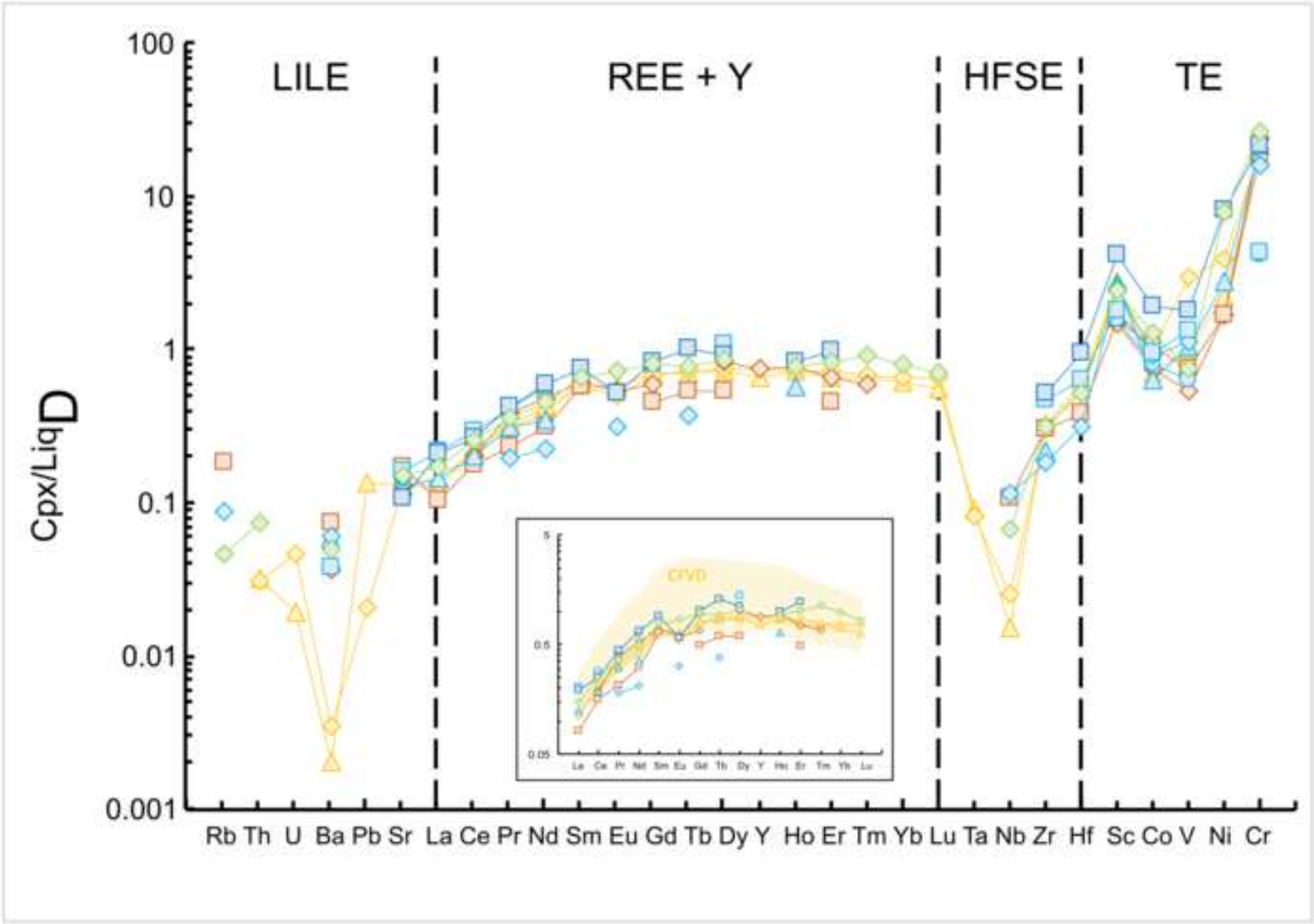

Figure 6

Click here to access/download;Figure;Figure 6.png

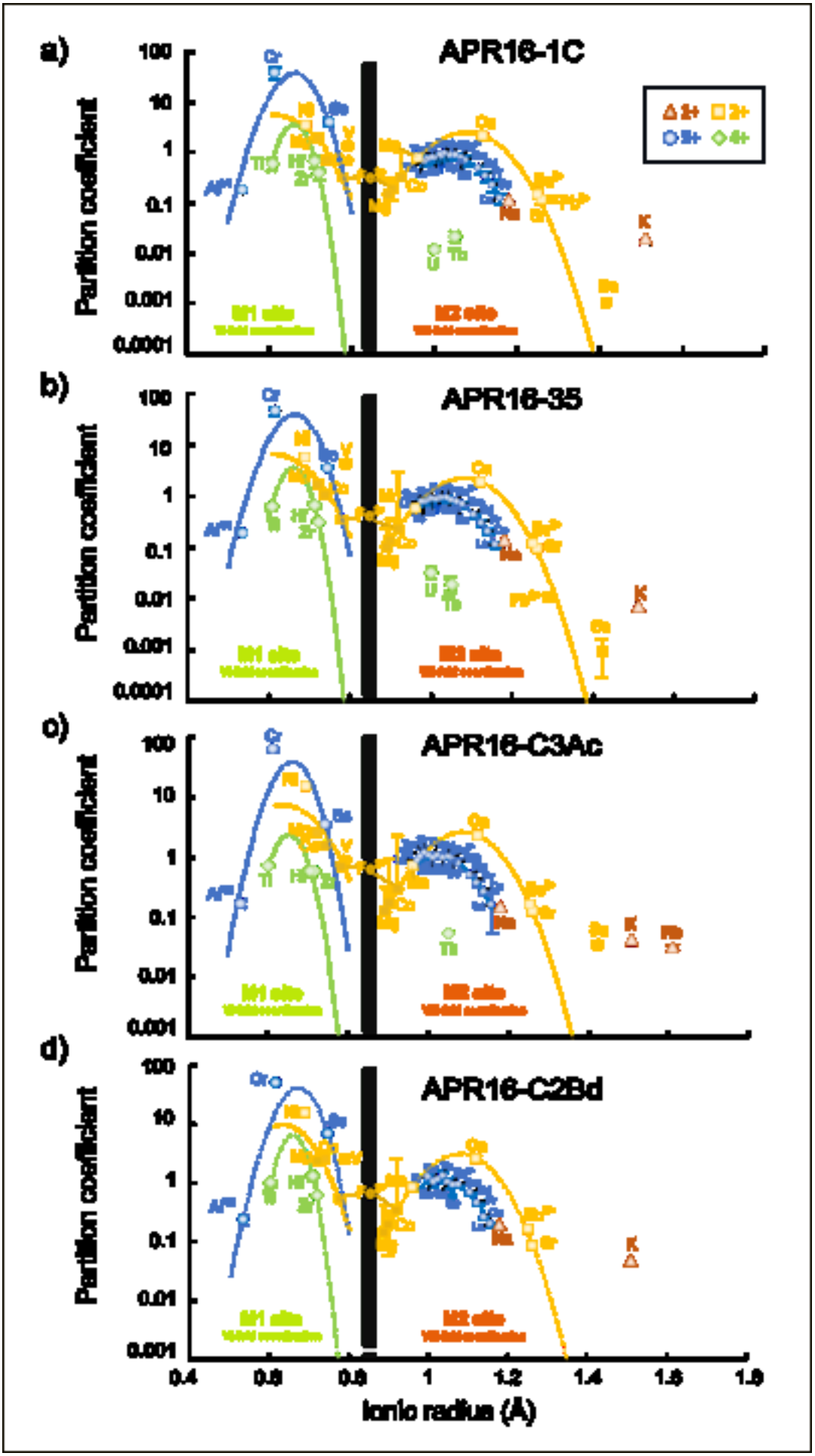

Figure 7

Click here to access/download;Figure;Figure 7.png

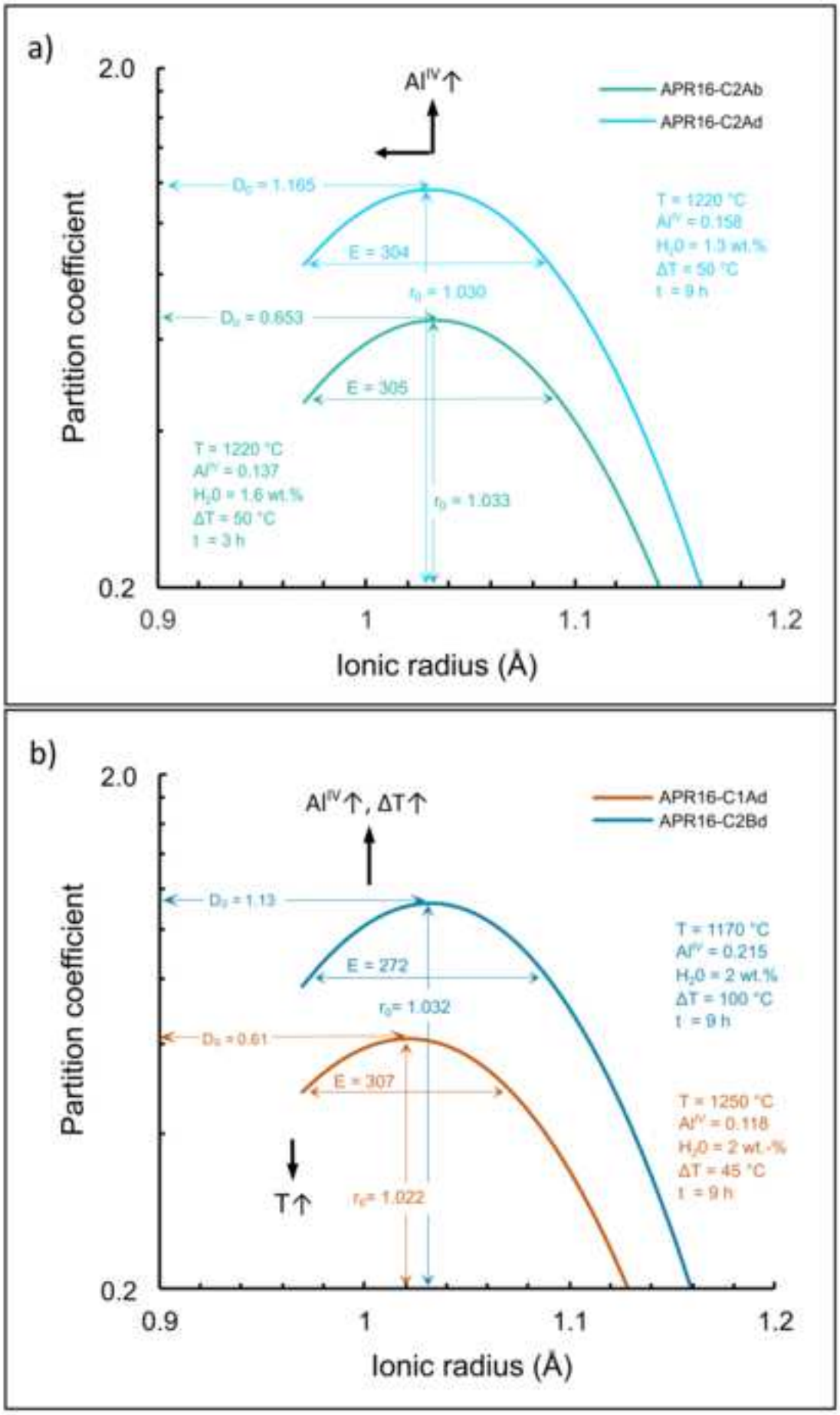

Figure 8

Click here to access/download;Figure;Figure 8.png

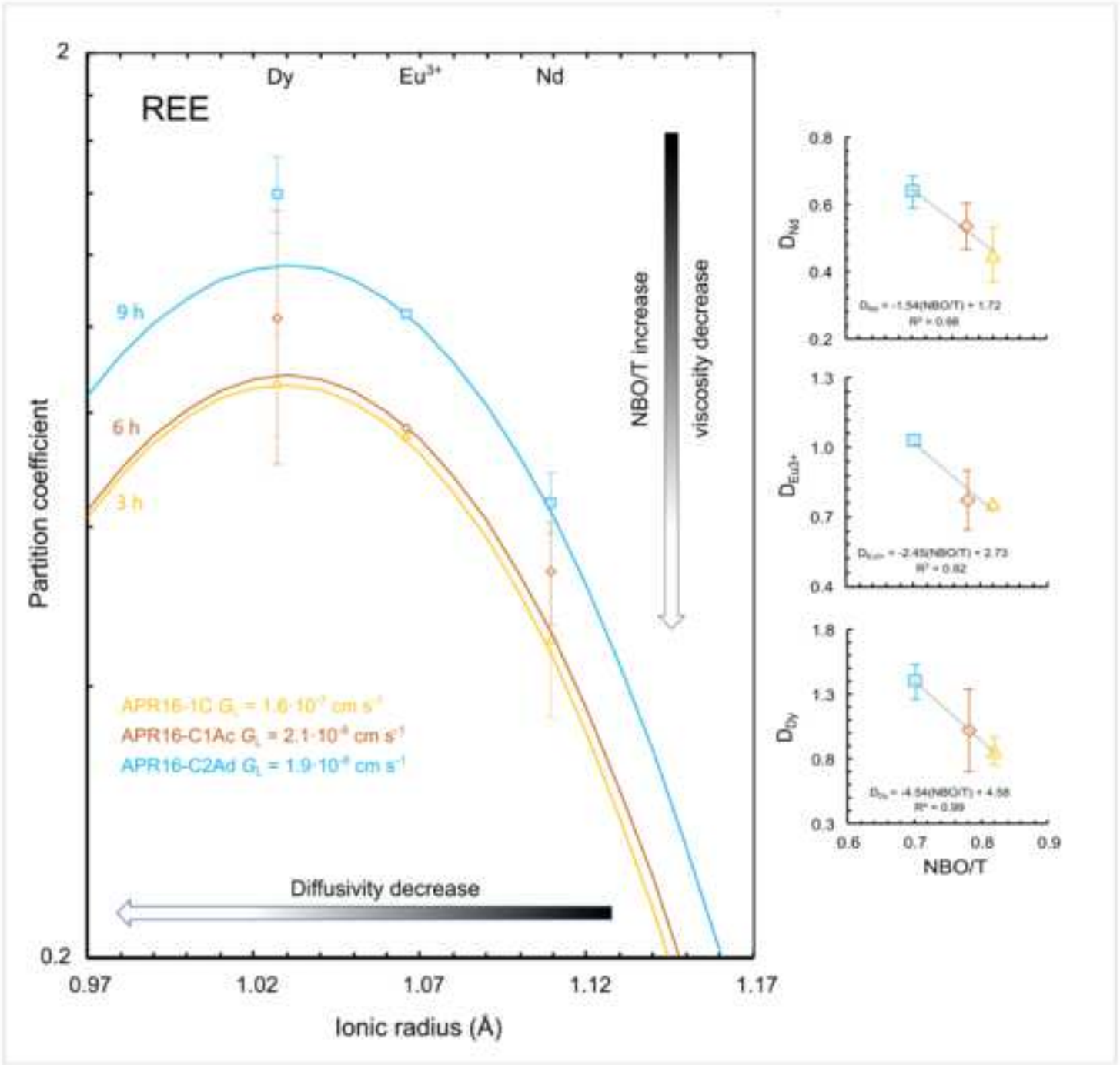

Figure 9

Click here to access/download;Figure;Figure 9.png

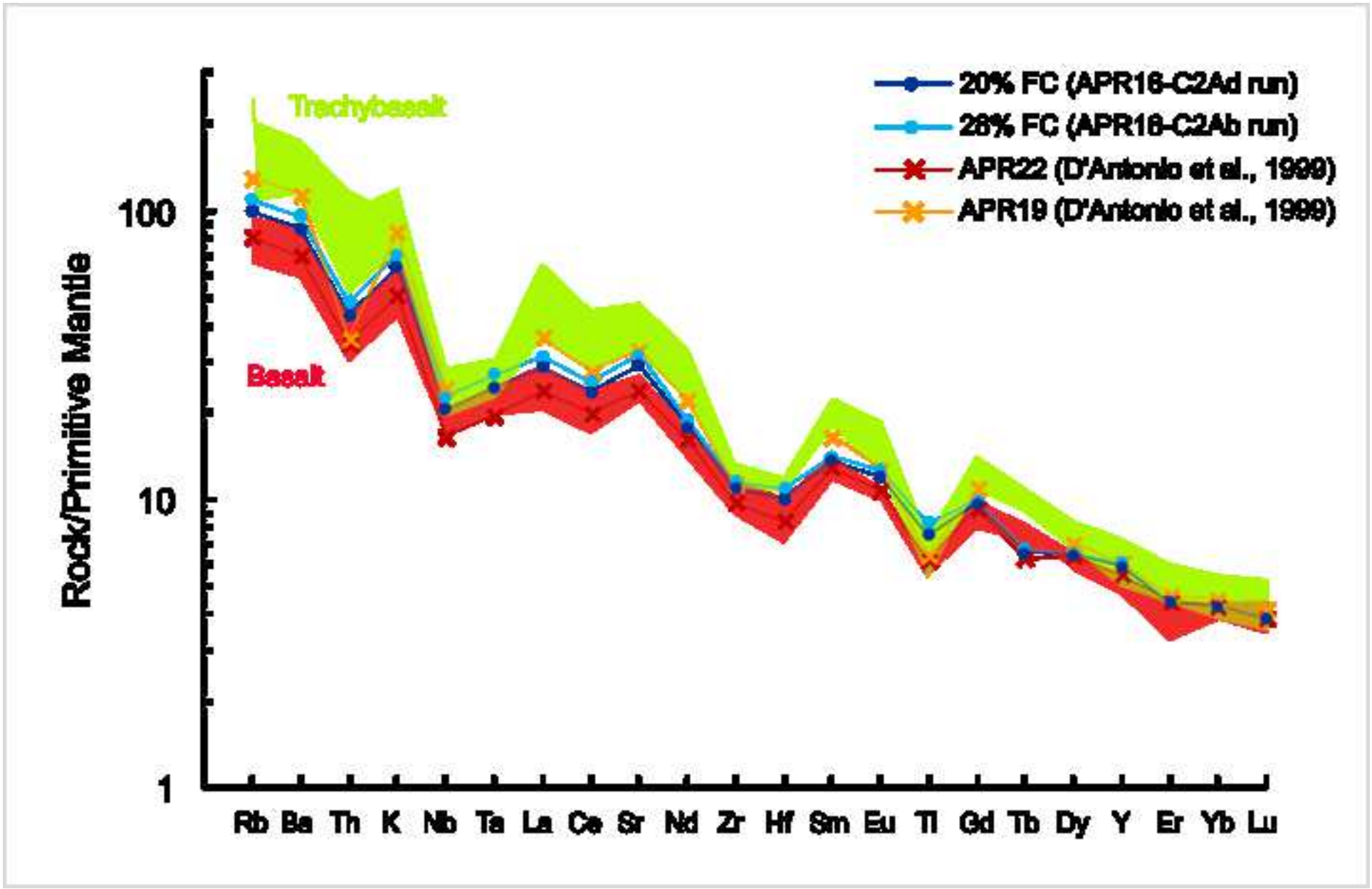

Supplementary Material 2 - Tables

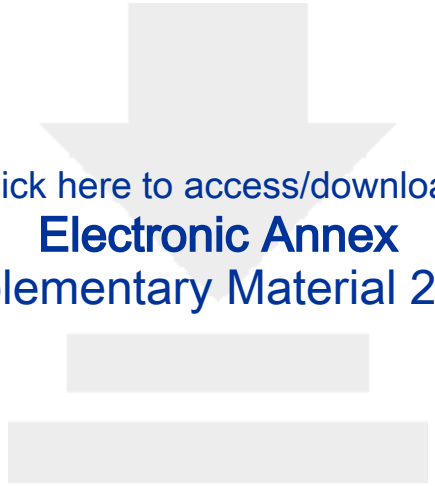

Click here to access/download

Electronic Annex

Supplementary Material 2..xlsx

Supplementary Material 3 - Figures

Click here to access/download

Electronic Annex

Supplementary material 3.pdf